

Natural and Forced Characteristics of Circular and Elliptic Jet Diffusion Flames

*A Report submitted
in partial fulfilment for the Degree of
Bachelor of Technology
in
Aerospace Engineering
by*

**Priy Devvrat Singh
(SC14B040)**

pursued in

Department of Aerospace Engineering

Indian Institute of Space Science and Technology

to



**INDIAN INSTITUTE OF SPACE SCIENCE AND TECHNOLOGY
THIRUVANANTHAPURAM**

April 2018

CERTIFICATE

This is to certify that the report entitled "**Natural and Forced Characteristics of Circular and Elliptic Jet Diffusion Flames**" submitted by **Priy Devrat Singh**, to the Indian Institute of Space Science and Technology, Thiruvananthapuram, as part of Project work is a bona fide record of the work carried out by him under our supervision from January 1, 2018 to May, 2018.

Dr. B. R. Vinoth

Place: IIST, Thiruvananthapuram
May 2018

Thesis Supervisor
Associate Professor
Department of Aerospace Engineering

Dr. Mahesh S.

Thesis Supervisor
Assistant Professor
Department of Aerospace Engineering

Dr. Manoj T. Nair

Head of the department
Department of Aerospace Engineering

Declaration

I declare that this thesis titled "**Natural and Forced Characteristics of Circular and Elliptic Jet Diffusion Flames**" submitted in completion of the Project work January - May 2018 is a record of original work carried out by me under the supervision of **Dr. B.R. Vinoth** and **Dr. Mahesh S.**, and has not formed the basis for the award of any degree, diploma, fellowship or other titles in this or any other Institution or University of higher learning. In keeping with the ethical practice in reporting scientific information, due acknowledgments have been made wherever the findings of others have been cited.

Place: IIST, Thiruvananthapuram
May 2018

Priy Devvrat Singh
SC14B040

Acknowledgements

A small step in the field of research requires innovation, support and expert guidance. First and foremost I would like to thank my mentors Dr. B.R. Vinoth and Dr. Mahesh S. for constantly guiding me throughout the project.

I am thankful to Arun B. Nair, PhD student in Aerospace department IIST, for all the technical help with experimental setup and spending his valuable time for discussion and assistance without which the experiment would have been impossible. I also would like to thank Mr. Nasurdeen and Mr. Ashwin for all the help with the experimental setup.

I am also grateful to my friends Chinatan Panigrahi, Nitish Kovalam, Priyanka Sahu, Vishwendra Pratap Singh, who helped me at various point of this project and without whom this would have been a lot difficult journey.

Lastly, I would like to thank my family and my friends who constantly supported and motivated me in the ups and downs of this journey.

Abstract

This experimental study is focused on understanding the characteristics of the natural and acoustically excited circular and elliptic jet diffusion flame. A high speed schlieren flow visualization technique was used to capture the time resolved flame response. Time series data was extracted from schlieren images for analysis which includes local decomposition techniques like Fast Fourier Transform, Spectrogram. The modal data-based global decomposition technique - Dynamic Mode Decomposition was applied to time resolved frames to get more insight into the spatial characteristics of the different modes of flame flickering in natural as well as forced response cases. Non-linear time series analysis was used to understand topology of the dynamics caused by interaction of thermal and acoustic fields.

Jet diffusion flame are hydro-dynamically globally unstable and they oscillate at their own natural frequencies. Experiments were carried out in order to compare the dependence of this frequency on velocity change for AR = 1, 2, 3 nozzles and it was found that the AR = 3 nozzle flame is the least sensitive to velocity change whereas AR = 1 has most dependency. Flames from all three nozzle were found to have positive influence of change of velocity on flickering frequency.

A scaling was also found through which the correlation between Strouhal number and Froude number collapsed for all three nozzle flames. Characteristic length for this scaling was equal to the minor diameter of nozzle, which strongly suggested that this hydrodynamic instability depends only on the minimum distance between shear layer, i.e, the minor axis length. This was not seen in case of typical ellipse scaling where $D = 2\sqrt{ab}$.

In order to understand the forcing response of flames, a speaker attached to the base of settling chamber was used to sinusoidally excite the flame. Both circular and elliptical (AR = 2, 3) flames were excited near natural oscillation frequency, near first subharmonic, near first super-harmonic of fundamental frequency. Different states like period-2 oscillations, quasi-periodicity, mode locked were observed when excited at different frequencies and amplitudes. When excited near the fundamental frequency all three flames showed similar response of getting locked in to forcing frequency as amplitude of acoustic signal was increased. A significant change in dynamics was observed between circular and elliptic nozzle flame when they were forced near the first subharmonic of fundamental frequency. Circular flame showed

period-2 oscillations at lock-in whereas elliptic flame got locked in through a mode locked state.

Table of contents

List of figures	xiii
List of tables	xvii
Nomenclature	xix
1 Introduction	1
1.1 Global Oscillations	1
1.2 Literature Review	2
1.3 Motivation and Aim	4
1.4 Dissertation Overview	5
2 Data and Signal Analysis Techniques	7
2.1 Fourier Transform	7
2.1.1 Discrete Fourier Transform	7
2.1.2 Limitations of Fourier Transform	8
2.2 Dynamic Mode Decomposition (DMD)	8
2.2.1 DMD General description	9
2.2.2 Algorithm	10
2.3 Non-linear Time Series Analysis	12
2.3.1 Phase-space Reconstruction:	12
2.3.2 Selecting the optimum time lag τ	13
2.3.3 Selecting the embedding dimension (d)	15
2.3.4 Poincaré Section (First return map)	17
2.3.5 Recurrence Plot	18
3 Experimental Methods	21
3.1 Experimental setup	21
3.1.1 Data Acquisition - DAQ	22

3.1.2	Flow supply and acoustic system	22
3.2	Optical flow visualization	23
3.2.1	Schlieren Visualization	23
3.3	Image Processing	25
3.4	Precautions implemented during experiment	26
4	Natural Characteristics of Circular and Elliptic Diffusion Flame	29
4.1	General Characteristics	30
4.2	Unsteady characteristics of flame	32
4.2.1	Temporal variation of flickering frequency	32
4.2.2	Spatial variation of flickering frequency	34
4.3	Results from non-linear time series analysis	35
4.4	Results from DMD	36
4.5	Effect of aspect ratio on flickering frequency	39
5	Forced Characteristics of Circular and Elliptic Diffusion Flame	45
5.1	Forced response of circular nozzle flame	46
5.1.1	Forcing near the fundamental : F_n	46
5.1.2	Forcing near the first subharmonic : $F_n/2$	48
5.1.3	Forcing at $F_f/F_n = 0.8454$ or $F_f = 10.5$ Hz	50
5.2	Forced response of elliptic nozzle flame	52
5.2.1	Forcing near the fundamental : F_n	52
5.2.2	Forcing near the first subharmonic : $F_n/2$	54
5.3	Results from DMD	57
6	Summary and Conclusion	59
6.1	Summary	59
6.2	Future Scope	61
References		63
Appendix A	Additional non-linear time series analysis tools	67
A.0.1	Lyapunov Exponent	67
Appendix B	Experimental parameters for natural oscillations case.	71

List of figures

2.1	Flowchart of non-linear time series analysis procedure.	12
2.2	Schematic of Poincaré map formation from phase space trajectory. (Juniper and Sujith, 2017)	17
3.1	Schematic of the experimental setup.	22
3.2	Schematic of Z type schlieren setup.	24
3.3	Representation of procedure to obtain time series data of schlieren emission at $x/D = 10$ location. The same procedure is applied to any other location needed for analysis.	26
4.1	Variation of schlieren flow field with flow rate for $AR = 3$ elliptic flame. . .	30
4.2	Image sequence of natural oscillations as seen from major axis side for flame with $AR = 3$ elliptic nozzle at flow rate of 0.9 SLPM ($Re = 219.53$), which has natural oscillation frequency = 11.26 Hz. The sequence runs from left to right, and the images are separated by 1/8 and 1/4 of time period of global oscillations in direct and schlieren visualization respectively. The red arrow indicates the location $x/D = 10$ at which time-series data was extracted for further analysis.	31
4.3	(a) Time series signal and (b) FFT of time series signal obtained at $x/D = 10$ for $AR=2$ elliptic nozzle with $Re = 239$	33
4.4	Waterfall and Spectrogram plots for $AR = 2$, $Re = 239$, natural oscillations case.	33
4.5	Power spectrum plot of signal at $x/D = [5,10,15,20,25,30,35,40]$ locations. The sequence moves from bottom to top. The spectrum peaks are at frequency = 11.73 Hz and its super-harmonics.	34
4.6	Non-linear time series analysis plots for $AR=2$, $Re = 239$, major side case. .	35
4.7	(a) Actual flow field snapshot and (b) region of the field selected for DMD analysis.	36

4.8	(a) DMD spectrum and (b) Eigenvalue visualization for flame with AR = 2 nozzle, Re = 239, major side visualization.	37
4.9	Spatial characteristics of mean and first 2 DMD modes for AR=2, Re = 239, major axis side case.	38
4.10	(a) Strouhal number vs Froude number, (b) Strouhal number vs Reynolds number for natural oscillations in case of AR = 1, 2, 3 nozzles. The characteristic length D is $2\sqrt{ab}$	41
4.11	(a) Strouhal number vs Froude number, (b) Strouhal number vs Reynolds number for natural oscillations in case of AR = 1, 2, 3 nozzles. The characteristic length D is $2a$	43
4.12	(a) Strouhal number vs Froude number, (b) Strouhal number vs Reynolds number with a common power law fit for natural oscillations in case of AR = 1, 2, 3 nozzles. The characteristic length D is $2b$	44
5.1	(a) Time series (b) power spectrum of intensity for circular flame forced at $F_f = 11.8$ Hz, slightly below the natural frequency, $F_n = 12.42$ Hz: $F_f/F_n=0.95$. Data shown for five forcing amplitude ($0.025V \leq A \leq 0.125V$) and for the unforced case at $x/D = 10$ location. The amplitude shown is in mV.	47
5.2	(a) 3D phase portrait (b) Poincaré map for circular flame forced at $F_f = 11.8$ Hz, slightly below the natural frequency, $F_n = 12.42$ Hz: $F_f/F_n=0.95$. Data shown for three forcing amplitude in range $0.025 \leq A \leq 0.125$ and for the unforced case at $x/D = 10$ location. $A_{loc} = 50$ mV	48
5.3	(a) Time series (b) power spectrum of intensity for circular flame forced at $F_f = 13.5$ Hz, slightly above the natural frequency, $F_n = 12.42$ Hz: $F_f/F_n=1.0869$. Data shown for five forcing amplitude ($0.025V \leq A \leq 0.125V$) and for the unforced case at $x/D = 10$ location. The amplitude shown is in mV. .	49
5.4	(a) Time series (b) power spectrum of intensity for circular flame forced at $F_f = 6.5$ Hz, slightly above the first subharmonic of natural frequency, $F_n = 12.42$ Hz: $F_f/F_n= 0.523$. Data shown for five forcing amplitude ($0.10V \leq A \leq 0.45V$) and for the unforced case at $x/D = 10$ location. The amplitude shown is in mV. $A_{loc} = 300$ mV	49
5.5	(a) 3D phase portrait (b) Poincaré map for circular flame forced at $F_f = 6.5$ Hz, slightly above the first subharmonic of natural frequency, $F_n = 12.42$ Hz: $F_f/F_n=0.523$. Data shown for five forcing amplitude in range $0.1V \leq A \leq 0.35V$ and for the unforced case at $x/D = 10$ location. $A_{loc}= 300$ mV	51

5.6 (a) Time series (b) power spectrum of intensity for circular flame forced at $F_f = 10.5$ Hz: $F_f/F_n = 0.523$. Data shown for five forcing amplitude ($0.10V \leq A \leq 0.70V$) and for the unforced case at $x/D = 10$ location. The amplitude shown is in mV.	52
5.7 (a) 3D phase portrait (b) Poincaré map for circular flame forced at $F_f = 10.5$ Hz: $F_f/F_n = 0.8454$. Data shown for 5 forcing amplitude in range $0.1 \leq A \leq 0.7$ and for the unforced case at $x/D = 10$ location.	53
5.8 (a) Time series (b) power spectrum of intensity for flame 2 (elliptic AR = 2 nozzle) when forced at $F_f = 12.6$ Hz: $F_f/F_n = 1.0742$. Data shown for five forcing amplitude ($0.05V \leq A \leq 0.20V$) and for the unforced case at $x/D = 10$ location. The amplitude shown is in mV. Lock-in occurs at $A_{loc} = 100$ mV .	54
5.9 (a) 3D phase portrait (b) Poincare map for flame 2 (AR = 2, Re = 239) forced at $F_f = 12.6$ Hz: $F_f/F_n = 1.0742$. Data shown for lock-in, before lock-in amplitude and for the unforced case at $x/D = 10$ location.	55
5.10 (a) Time series (b) power spectrum of intensity for flame 3 (elliptic AR = 3 nozzle) when forced at $F_f = 6.1$ Hz: $F_f/F_n = 0.5417$. Data shown for five forcing amplitude ($0.1V \leq A \leq 0.7V$) and for the unforced case at $x/D = 10$ location. The amplitude shown is in mV. Lock in occurs at $A_{loc} = 700$ mV .	56
5.11 (a) 3D phase portrait (b) Poincaré map for flame 3 (AR = 3, Re = 219.52) forced at $F_f = 6.1$ Hz: $F_f/F_n = 0.5417$. Data shown $A = 400, 700$ mV and for the unforced case at $x/D = 10$ location.	56
5.12 (a) DMD spectrum, (b) eigenvalue visualization for flame 1 when forced at $F_f = 6.5$ Hz and $A = 100$ mV.	57
5.13 Spatial characteristics of mean, natural and forcing modes for AR=1, Re = 295.74, major axis side case.	58
A.1 Illustration of procedure for calculating Lyapunov exponent. Taken from Wolf et al. (1985)	68

List of tables

3.1	Details about schlieren optical setup components	25
4.1	Camera settings used to capture natural oscillations schlieren imaging	29
4.2	Experimental parameter for natural oscillations study	32
4.3	Power law fit for $D = 2\sqrt{ab}$	40
4.4	Power law fit for $D = 2a$	42
4.5	Power law fit for $D = 2b$	42
5.1	Camera settings for acoustic excitation case	45
5.2	All flames used for acoustic excitation	46
B.1	Experimental parameters with $D = 2\sqrt{ab}$ for natural oscillations. Bold indicated cases are the ones selected for acoustic excitation.	71

Nomenclature

Acronyms / Abbreviations

- DFT Discrete Fourier Transform
FFT Fast Fourier Transform
DMD Dynamic Mode Decomposition
POD Proper Orthogonal Decomposition
SVD Singular Value Decomposition
DM Dynamic Mode
SLPM Standard Liter Per Minute
FPS Frames Per Second

Other Symbols

- F_f Forcing Frequency
 F_n Natural Frequency
 A Forcing Amplitude
 A_{loc} Lock-in Amplitude
 τ Time Lag

Chapter 1

Introduction

1.1 Global Oscillations

A system is said to possess global oscillations when the whole of it executes coherent oscillations in time in all stream-wise locations. Unless energy is supplied continuously, the oscillations decay with time and eventually die out. Based on the source of energy, the global oscillations are classified into self-excited flows and externally excited flows. In the self-excited flows, the energy needed to sustain the dynamical state is provided by the flow itself. The self-excited flows can further be broadly classified based on the medium through which the energy is fed back to the flow. The different types of feedback are hydrodynamic, elastic and acoustic. Global self-excited oscillation can be found in both reacting and non-reacting flows. Some examples are flickering of a candle flame, vortex shedding in bluff body wakes, low density jets.

A necessary condition for global instability, though, is the presence of a finite region of absolute instability. The key concept is that absolute instability enables perturbations to grow both upstream and downstream, whereas convective instability enables perturbations to grow downstream only. A flow that is convectively unstable everywhere, therefore, acts as a spatial amplifier of external perturbations. A flow that is absolutely unstable over a sufficient region, by contrast, acts as an oscillator. ([Li, 2012](#))

The cause of thermoacoustic instability is the resonant interaction that occurs between unsteady combustion and acoustics. Even infinitesimal fluctuations in heat release from a flame can cause the reacting gases to expand and contract cyclically, propagating initially weak acoustic waves to the surroundings. On interacting with the combustor, these waves may partially reflect back to perturb the flame. Thermoacoustic instability is a serious problem because it is difficult to predict and control. If left unchecked it can induce flame blow-off or flashback, trigger thrust and power variations, and enhance heat transfer to the combustor

walls. Over time it can even impart sufficient cyclic loading to structural components to cause catastrophic fatigue failure. According to [Li \(2012\)](#) If the Rayleigh integral¹ is positive, an acoustic wave gains energy from the flame, becoming excited. If it is negative, the acoustic wave loses energy to the flame, becoming damped. If it is zero, no net energy is exchanged over a full oscillation period.

Diffusion flames are hydro-dynamically globally unstable in nature and they oscillate at their natural frequency. The flame oscillation frequency is dominated by buoyancy-driven instability and correlated with large toroidal structures outside the visible flame zone. Previous work has suggested that flows with global instability are universally characterized by self-excited oscillations at discrete natural frequencies and by insensitivity to external disturbances imposed at other frequencies. This features for circular flames was explored experimentally by [Li \(2012\)](#) and [Juniper et al. \(2009\)](#), they reported that the dynamics of globally unstable flames is much richer than that and resembles the dynamics of non-linear oscillators.

This thesis is part of an overall research effort to investigate how hydrodynamic oscillations interact with acoustic oscillations in case of elliptical diffusion flames, and whether the former can be used to weaken/control the latter. To understand and compare any change in dynamics the same experiments were also carried out for circular flame also. In our simple experimental configuration, we will attempt to study the fundamental dynamics associated with thermo-acoustic instability.

1.2 Literature Review

Diffusion flame are the class of flows that possess global oscillations, and it has been extensively studied in combustion community from decades. It is found by [Hamins et al. \(1992\)](#) and [Wang et al. \(2012\)](#) that laminar diffusion flames have a typical flickering/oscillating behavior at a low frequency range of 10-20 Hz. The flame flickering frequency in case of circular nozzle is relatively independent of fuel type, nozzle diameter and jet exit velocity. In a flickering flame ([Hamins et al., 1992](#)), the flame and flow interactions show periodic and reproducible characteristics. The flame oscillation frequency is dominated by buoyancy-driven instability and correlated with large toroidal structures outside the visible flame zone.

According to [Cetegen and Dong \(2000\)](#) a diffusion flame exhibits two modes of oscillations - varicose and sinuous. The preference of mode depends on many flow parameters like Froude number, Reynolds number etc, which are discussed in detail in [Cetegen and Dong](#)

¹Rayleigh was the first to scientifically explain the physical mechanism by which a heat source can transfer energy to an acoustic field

(2000). The buoyancy induced instability in case of varicose mode results in axisymmetric contractions and expansions of the flame front leading to formation of toroidal vortical structures and flame tip cutting and hence fluctuations (Fig.4.2), while the unstable flames in the sinuous mode have a very steady contracting flame envelope near the nozzle and the instability develops further downstream causing the flame to meander in a sinuous mode and it does not cause any flame tip oscillations. Area of interest for present study is varicose mode of oscillations.

Baird (2005) paper investigated the effect of burner geometry on partially premixed jet flames and reported the shorting of the flame length due to flame splitting into two sub-flames along major axis for AR = 4, while the laminar flames were similar in appearance till AR = 3. Reduction in flame length comes with increase in CO emission and a loss of stability. Gollahalli et al. (1992) compared the stability of flame, soot radiation, temperature profile, CO, NO emission for flames from circular and elliptic nozzles.

The essential component of a combustion system, the flame, is a complex entity capable of exhibiting elaborate nonlinear behavior, as reported in several previous investigations (Balusamy et al., 2015; Golub and Krivokoritov, 2015; Hallberg and Strykowski, 2008; Juniper et al., 2009; Kabiraj et al., 2012; Kabiraj and Sujith, 2012; Li, 2012). According to the literature the interaction between unsteady heat release of combustion process and acoustics field can result in complex and rich dynamics of thermoacoustic oscillations, which is often observed in other naturally occurring non-linear systems.

Depending on the frequency and magnitude of the acoustic field the nonlinear interaction between acoustic and self excited systems can be used to control/diminish the thermoacoustic instability. Hallberg and Strykowski (2008) reported the effect of acoustic on helium jet perturbation was diminished for some particular acoustic parameters while it was enhanced for some other cases. The dynamics of small AR elliptic nozzle jets and flames were studied experimentally by Lin and Chang (1998) and it was found that the axis switching points shifts upstream when the jet is excited acoustically. Krivokorytov et al. (2012) investigated the acoustic action on diffusion flame in terms of content of soot, nitrogen oxide and in increase in the efficiency of fuel combustion. In addition, the acoustic action in individual cases can lead to the effect of flame bifurcation.

Li (2012), Li and Juniper (2013) investigated the response of weaker and stronger circular diffusion flame when excited sinusoidally near the fundamental frequency of flame. Main objective of their research was to see lock in behavior and the type of bifurcation and route to lock in. They also compared lock in amplitude/curve for different flame by weakening the global instability of flame using (1) co-flow, (2) by diluting CH_4 with N_2 . They concluded

that the flames with weaker global instability has low lock in amplitude. They also compared their results with a numerically solved van-der poll oscillator.

[Kabiraj and Sujith \(2012\)](#) investigated the nonlinear transition undergone by thermo-acoustic oscillations to flame blowout via intermittency, in response to variation in the location of the combustion source with respect to the acoustic field of the confinement. A review of non-linear time series analysis techniques is provided in [Juniper and Sujith \(2017\)](#). [Kabiraj et al. \(2012\)](#) shows that a nonlinear time series analysis of acoustic pressure data enables the identification of nonlinear states and the sequence of bifurcations followed by the system.

Dynamic Mode Decomposition

This technique was first introduced to the fluids community in 2008, subsequently followed up with an archival paper by Schmid ([Schmid et al., 2010](#)) and it has quickly gained a following in fluid engineering. The connections with the Koopman operator were given in [Rowley et al. \(2009\)](#), which explains the meaning of DMD for a nonlinear system (see also the review articles by [Mezić \(2013\)](#) and [Tu, Rowley, Kutz and Shang \(2014\)](#)). There have been a number of different formulations and interpretations of DMD since then which are mentioned in [Taira et al. \(2017\)](#).

1.3 Motivation and Aim

Part of the motivation came from [Lin and Chang \(1998\)](#) in which they studied elliptical jets and flames. Our study also focuses on elliptical flames because of its high potential for use in engineering applications.

Studies of asymmetric jets have been reported as early as 1966, These rectangular jet studies noted the phenomenon of axis switching, where instability in the minor axis of the jet spreads more rapidly than in the major axis. Other early asymmetric jet studies were motivated by the use of a rectangular nozzle for thrust augmentation and noise reduction in aircraft engine exhaust systems. Applications of excited elliptic jets and flames are for enhanced mixing and chemical reactions, and control of aerodynamic noise.

Nonlinear self-excited thermoacoustic oscillations appear in systems involving confined combustion in the form of coupled acoustic pressure oscillations and unsteady heat release rate. Thermoacoustic instability is a consequence of a positive feedback between the acoustic field of the system and the unsteady heat release rate from combustion. Such a configuration is the most basic combustion-driven thermoacoustic system. In our simple experimental

configuration, we have attempted to study the fundamental dynamics associated with thermoacoustic instability. Effect of acoustic field on circular diffusion flames were reported by [Li \(2012\)](#), This thesis explores the same dynamics but mainly in case of circular and elliptic nozzle flames.

1.4 Dissertation Overview

The organization of the report is as follows : Chapter 2 talks about all the data and signal analysis techniques used to analyze data in the scope of this project. It mainly includes local and global decomposition techniques and techniques available for time series analysis. Chapter 3 includes details about experimental setup and methods used in order perform experiment and acquire data. Chapter 4 discusses the results obtained related to natural characteristics of circular and elliptic flame. Chapter 5 discusses the results obtained related to the acoustically forced characteristics of circular and elliptic flames. Finally the chapter 6 represent a summary and conclusion of the study and some direction for the future work.

Chapter 2

Data and Signal Analysis Techniques

This Chapter is concerned with review of local decomposition techniques like Discrete Fourier Transform (DFT) and Fast Fourier Transform (FFT) algorithm following that it includes the global decomposition technique Dynamic Mode Decomposition and its algorithms to implement, followed by advantages and limitations of each method. The last part of this chapter includes details about the techniques used for non-linear time series analysis which gives us more insight into the topology of the system studied.

2.1 Fourier Transform

The aim of Fourier Transform is to obtain the frequency spectrum of the signal. A continuous periodic signal $x(t) = x(t + T)$ with the period T can be decomposed into an infinite series of sinusoidal functions (Fourier series), whose linear combination reproduces the original function.

2.1.1 Discrete Fourier Transform

Since the data obtained from simulation or experiment is discrete so we are interested in Discrete Fourier Transform which is defined as - a finite series of complex values $x_n = x(t = n\Delta t_s)$ with $n = 0, 1, \dots, N-1$, sampled at equal time intervals and over the time duration $0 < t < T = N\Delta t_s$ can be decomposed into a finite sum of complex Fourier coefficients X_k , yielding the Discrete Fourier Transform (DFT) (followed from [Tropea et al. \(2007\)](#))

$$X_K = FT(x_n) = \sum_{n=0}^{N-1} x_n \exp\left(\frac{-2i\pi nk}{N}\right) \quad (2.1)$$

Two properties of the DFT deserve particular attention.

- According to Nyquist sampling theorem, the maximum resolvable frequency is half the sampling frequency $f_{max} = f_s/2$ and the resolution is determined by the data set duration $\Delta f_s = 1/T$.
- Since the time between the sample points is not infinitely small, the power in the signal at frequencies above f_{max} will appear at lower frequencies, an effect known as aliasing. ([Tropea et al., 2007](#))

In practical implementations of the DFT (2.1) is not used directly but rather a recursive form known as the fast Fourier Transform (FFT) is used. There are many realizations of the FFT, but they share one feature in common, namely, that they normally operate on 2^n points: sample records are restricted to values such as 16, 32, 64, 128, . . . The calculation time of the DFT (2.1) implemented with increases with N^2 . The FFT algorithm reduces the computation time to the order of $N \log(N)$. Algorithms exist for FFTs using other record lengths, especially prime number decompositions; however, these are not in widespread use. For more insight on FFT the reader is encouraged to refer to [Strang \(2003\)](#).

2.1.2 Limitations of Fourier Transform

- These techniques can only be applied to time series of data obtained at a point in domain of interest.
- It is not possible to analyze the flow field globally using these techniques.
- Loss of the time information in frequency domain. Although it is possible to determine the frequencies present, it is impossible to determine the exact time at which these oscillations occur, hence this method is only limited to stationary signals.
- These methods require a predefined basis functions.

2.2 Dynamic Mode Decomposition (DMD)

Dynamic Mode Decomposition (DMD) provides a means to decompose time-resolved data into modes, with each mode having a single characteristic frequency of oscillation and growth/decay rate. DMD is based on the eigen decomposition of a best-fit linear operator that approximates the dynamics present in the data. ([Taira et al. \(2017\)](#))

Moreover, as DMD is purely a data-driven algorithm without the requirement for governing equations, it has been widely applied beyond fluid dynamics: in finance, video processing, epidemiology, robotics, and neuroscience. As with many modal decomposition techniques,

DMD is most often applied as a diagnostic to provide physical insight into a system. The use of DMD for future-state prediction, estimation, and control is generally more challenging and less common in the literature.

2.2.1 DMD General description

The journal paper by [Schmid et al. \(2010\)](#) introduced basic DMD algorithm¹. It was formulated in terms of the companion matrix and helped in reducing very high-dimensional dynamic data into few coupled spatio-temporal modes. But because of its numerical instability, the SVD based DMD algorithm was presented by [Schmid \(2010\)](#) and was named as the standard DMD algorithm. Although it was generally accepted, again by [Tu, Rowley, Luchtenburg, Brunton and Kutz \(2014\)](#) this SVD-based approach was slightly modified and is now known as the exact DMD algorithm. Following section will discuss algorithms of exact DMD.

The DMD is based on the time-resolved sequence of flow field snapshots. Let v_j represent a general flow field data (a snapshot) at j^{th} time step where an equal time interval Δt is assumed between any snapshot v_j and v_{j+1} . Then sequence of N snapshots (from 1 to N) can be written as

$$V_1^N = \{v_1, v_2, v_3, \dots, v_N\}$$

Also assume a constant linear mapping A from one snapshot to the next. It is worth reminding that in experiments, the data is actually produced by a non-linear process. So it is assumed invoking a linear-tangent approximation from one snapshot to the next. So we can write

$$v_{j+1} = Av_j$$

Which can be extended to all the snapshots as

$$\{v_2, v_3, v_4, \dots, v_N\} = A\{v_1, v_2, v_3, \dots, v_{N-1}\}$$

or

$$V_2^N = AV_1^{N-1}$$

¹For basic DMD algorithm refer to [Schmid et al. \(2010\)](#)

2.2.2 Algorithm

DMD algorithms involve SVD based approach of the data sequence. let

$$Y = V_2^N$$

and

$$X = V_1^{N-1}$$

where

$$Y = AX$$

The next step is to compute SVD of X data matrix:

$$X = U \Sigma V^T \quad (2.2)$$

Projecting onto the POD modes:

$$\tilde{X} = U^T X$$

$$\tilde{Y} = U^T Y$$

Next step involves solving an optimization problem to minimize the prediction error:

$$\tilde{A} = \operatorname{argmin} \|\tilde{Y} - \tilde{A}\tilde{X}\|_F^2 \quad (2.3)$$

Which has an analytic solution:

$$\tilde{A} = \tilde{Y}\tilde{X}^\dagger = U^T Y V \Sigma^{-1} = U^T A U \quad (2.4)$$

Computing the eigenvalues and eigenvectors of \tilde{A} , we get

$$\tilde{A}W = \Lambda W \quad (2.5)$$

where Λ are the DMD eigenvalues of \tilde{A} .

DMD modes(ϕ) can be obtained as:

$$\Phi = UW \quad (2.6)$$

where each column of Φ is a DMD mode ϕ_i corresponding to eigenvalue λ_i

Amplitude (α) of the DMD modes is obtained by projecting the DMD modes on the first snapshot in the dataset:

$$\alpha = \Phi^\dagger X_1 \quad (2.7)$$

Where Φ^\dagger is the pseudo inverse of the Φ .

It should be noted that this method produces modes with unit norm since

$$\Phi\Phi^T = UWW^TU^T = 1$$

If desired, the DMD modes can be scaled in a number of ways, as described in Appendix A of [Tu, Rowley, Luchtenburg, Brunton and Kutz \(2014\)](#)

Finally, we may write an approximation of the observed data as a simple dynamic model $\widehat{X}(t)$,

$$\widehat{X}(t) = \Phi\Lambda^{i-1}\alpha \quad (2.8)$$

Where i varies from 1 to N (no. of snapshots in database). If the raw data X is strictly real valued, then we may consider only the real component of $\widehat{X}(t)$.

The eigenvalue λ_i corresponds to the temporal dynamics of the spatial mode ϕ_i . Specifically, its rate of growth/decay and frequency of oscillation are reflected in the magnitude and phase components of λ_i , respectively.

Define

$$\mu_i = \log(\lambda_i)/\Delta t \quad (2.9)$$

then growth rate of DMD modes is given by real part of μ and frequency corresponding to DMD modes is given by imaginary part of μ . The DMD spectrum is obtained by plotting frequency vs amplitude of each mode.

2.3 Non-linear Time Series Analysis

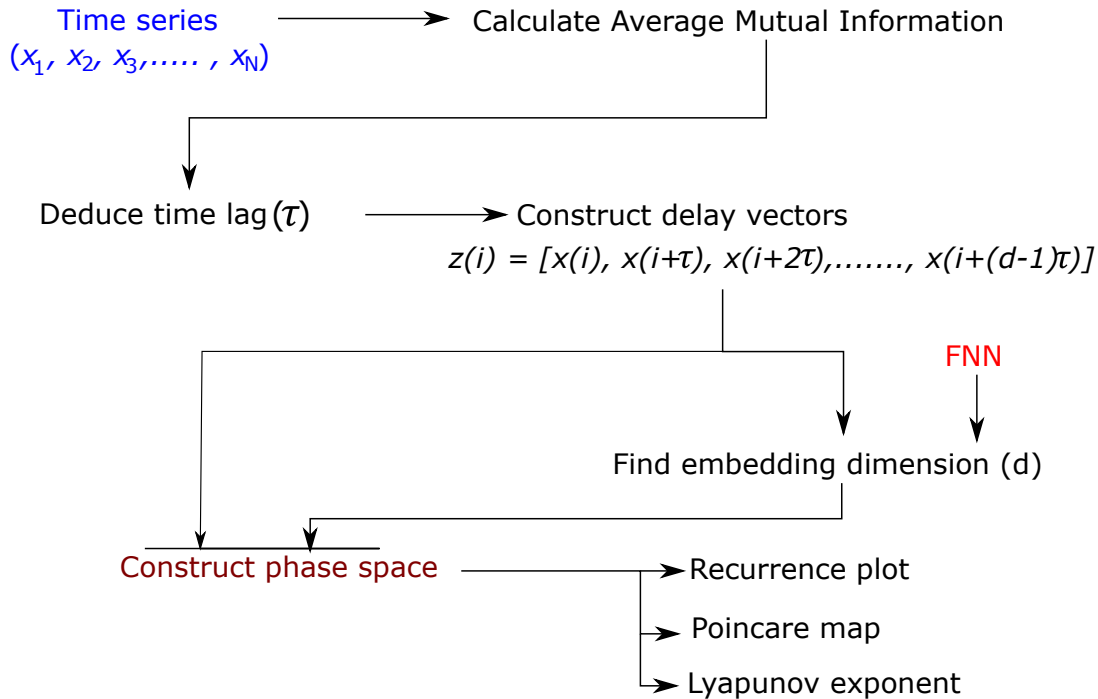


Fig. 2.1 Flowchart of non-linear time series analysis procedure.

2.3.1 Phase-space Reconstruction:

In mathematics and physics, a phase space of a dynamical system is a space in which all possible states of a system are represented, with each possible state corresponding to one unique point in the phase space.

Dynamical systems are systems that evolve with time. The dynamics of such systems at every instant of time can be appropriately determined from the available knowledge of fixed number of independent variables (also known as state variables) that characterize the system. The time evolution of these variables can be expressed in the form of a set of linear differential equations given by

$$\dot{X} = \phi(X) \quad (2.10)$$

where the dot represents the time derivative and the function ϕ comprises the overall form of dynamical evolution of that variable.

For a given set of initial conditions and the functional form, the future dynamical states of the system variable can be correctly determined from the above equation. The path traced by the sequence of points (also called states) obtained from the solution of this equation

is called the trajectory of the system dynamics. The evolution of this trajectory is often represented in a plot known as a phase portrait. A phase portrait is a plot between the number of independent variables that are required to signify the state of a system correctly. Phase space includes all possible states of the system dynamics. Some of the various types of dynamical motions exhibited by systems are Static equilibrium (Fixed point attractor), Periodic (limit cycle attractor), Quasi-periodic (Torus attractor) and chaotic motion (Strange attractor) etc. ([Juniper and Sujith, 2017](#))

For experimental and naturally occurring dynamical systems, the phase space and a mathematical description of the system are often unknown. Real systems are more complex and require an infinite number of dimensions to describe the state of a given dynamical system completely. In practice, the number of dynamical variables available from a given system is restricted to a few numbers, and in the limiting case, it is one. In such a situation, it is possible to construct a higher dimensional phase space, from the given knowledge of a single univariate observation, using a theorem of time delay embedding proposed by [Takens \(1981\)](#).

According to Takens delay embedding theorem ([Takens, 1981](#)), if we have a single observable time series $[x_1, x_2, x_3, \dots, x_N]$ measured at a particular value of the control parameter, we can embed the signal into a higher-dimensional phase space by choosing an appropriate value of time delay (τ) and embedding dimension (d). With this, the constructed delay-coordinate vectors are given by,

$$Z(i) = [x(i), x(i + \tau), x(i + 2\tau), \dots, x(i + (d - 1)\tau)]; \quad (2.11)$$

Where $i = 1, 2, 3, \dots, N-(d-1)\tau$

The plot between the elements of these vectors shows the evolution of the system dynamics in the d -dimensional phase space.

2.3.2 Selecting the optimum time lag τ

Theoretically, for infinite noise-free data, any arbitrary value of the successive measurement can be chosen as the optimum time delay, according to Takens embedding theorem. However, in reality, due to practical limitations such as finite data length, finite precision and the presence of noise, the choice of time delay is not straightforward. First, τ has to be large enough so that the information we get from measuring the value of x at time $i + \tau$ is significantly different from the information we already have by knowing the value of x at time i . Only

then will it be possible to gather enough information about all other system variables that influence the value of x to reconstruct the whole attractor. Second, τ should not be larger than the typical time in which the system loses memory of its initial state. In reality, we have finite equally sampled data with a sampling frequency of $1/\tau_s$ the delay should always be expressed in terms of multiples of sampling time (τ_s).

There are 2 ways to determine optimum time lag from a time series signal.

1. Autocorrelation function (ACF)

For a given time series data X_i sampled at equal intervals of time τ_s , the autocorrelation function at lag k is given by

$$r_k = \frac{\sum_{i=1}^{i=N-k} (X_i - \bar{X})(X_{i+k} - \bar{X})}{\sum_{i=1}^{i=N-k} (X_i - \bar{X})^2} \quad (2.12)$$

Where $i = 1, 2, 3, \dots, N$ and \bar{X} is the mean of the signal.

Time delay is selected as first zero crossing or the first minima of r_k . Limitation of this method is that this is based on linear theory and hence it only detects linear-independance of coordinates. For nonlinear systems, average mutual information is another measure which is often preferred over ACF for finding the optimum time delay, and is based on information theory.

2. Average Mutual Information (AMI)

The mutual information between x_i and $x_{i+\tau}$ quantifies the amount of information we have about the state $x_{i+\tau}$ presuming we know the state x_i .

Algorithm for AMI

1. Given a time series of the form $[x_1, x_2, x_3, \dots, x_N]$, first find out the minimum (x_{min}) and the maximum (x_{max}) of the sequence.
2. Divide the absolute value of difference $|x_{max} - x_{min}|$ into j equally sized intervals, where j is a sufficient large integer number.

3. Finally calculate the expression

$$I(\tau) = \sum_{h=1}^j \sum_{k=1}^j P_{h,k}(\tau) \log \frac{P_{h,k}(\tau)}{P_h P_k} \quad (2.13)$$

Where :

- P_h and P_k denote the probabilities that the variable assumes a value inside the h^{th} and k_{th} bins
- $P_{h,k}(\tau)$ is the joint probability that X_i is in bin h and $X_{i+\tau}$ is in bin k.
- First minima of $I(\tau)$ is optimal choice for τ

2.3.3 Selecting the embedding dimension (d)

Theoretically if we know the original dimension of the system, say m (known from the m-coupled differential equations of the system), then according to Takens embedding theorem , the $d > 2m$ dimension is sufficient to reconstruct the observed motion of the system. However, in reality, the governing equations of the system are unknown, and due to the unavailability of data for very large durations from the experiments, it is quite difficult to find the appropriate dimension of the unfolded attractor.

The dimension of the phase space should be large such that if the attractor is unfolded in the d-dimensional space, the neighbors of each trajectory of the reconstructed attractor have same neighbour as that observed in the d-1 phase space. These neighbors are the result of their geometric nature and not the artifact of their reconstruction in a smaller dimensional space.

The common methods used are :

Method 1 - False Nearest Neighbor (FNN)

The main idea of this method is to eliminate false crossings of the phase space trajectories, which may arise due to the projection of a higher dimensional original attractor into a lower-dimensional reconstructed phase space, and not due to their dynamics. The method of FNN measures the percentage of closeness, in terms of Euclidian distances, of neighboring points of the trajectory in a given dimensional space, and compares it with the next dimensional space. If the ratio of these distances is greater than a predefined threshold due to a change in the dimension, the neighbors of the trajectory are considered as false neighbors.

Let the dimension of an attractor be d , the time delay be τ , and the r^{th} nearest neighbor of reconstructed vector $y(n)$ is given by $y^r(n)$,

Euclidian distance between the points $y(n)$ and $y^r(n)$ is calculated as

$$R_d^2(i, r) = \sum_{k=0}^{k=d-1} [y(i+k\tau) - y^r(i+k\tau)]^2 \quad (2.14)$$

In $d+1$ dimensional space distance between these points become

$$R_{d+1}^2(i, r) = \sum_{k=0}^{k=d} [y(i+k\tau) - y^r(i+k\tau)]^2 \quad (2.15)$$

The criterion to detect false neighbor:

$$\frac{[R_{d+1}^2(i, r) - R_d^2(i, r)]^{0.5}}{R_d(i, r)} = \frac{|y(i+d\tau) - y^r(i+d\tau)|}{R_d(i, r)} > R_T \quad (2.16)$$

R_T is a threshold that decides the falseness of the nearest neighbors. Which is also a limitation of this method since for different values of R_T , the method will produce different values of the embedding dimensions (d).

Method 2 - Cao's method

To overcome the limitation of method of FNN for determining the optimum embedding dimension L cao¹ suggested another method where we define a new quantity $a(i, d)$ as follows,

$$a(i, d) = \frac{\|y_i(d+1) - y_{n(i,d)}(d+1)\|}{\|y_i(d) - y_{n(i,d)}(d)\|} \quad (2.17)$$

$y_i(d)$ is a i_{th} reconstructed vector in d dimensional space and $n(i, d)$ is the nearest neighbor of $y_i(d)$ in d -dimensional space.

$$y_i(d) = [x(i), x(i+\tau), x(i+2\tau), \dots, x(i+(d-1)\tau)]; \quad (2.18)$$

The mean of $a(i, d)$ is calculated as,

$$E(d) = 1/(N-d\tau) \sum_{i=1}^{i=N-d\tau} a(i, d) \quad (2.19)$$

¹Cao (1997)

The quantity $E(d)$ depends on the dimension d and the time delay τ . The variation of $E(d)$, as the value of dimension changes from d to $d+1$, is expressed in terms of new quantity

$$E1(d) = \frac{E(d+1)}{E(d)} \quad (2.20)$$

Here $E1(d)$ will stop changing once all the false neighbors are resolved after a dimension d_0 . Then, $d_0 + 1$ can be chosen as the minimum embedding dimension.

2.3.4 Poincaré Section (First return map)

A Poincaré section or map explores the properties of a continuous time system by lowering its phase space dimension. This is achieved by transversely cutting an m dimensional attractor of the system through an $m - 1$ dimensional plane. It reveals the various types of motion such as periodic, quasiperiodic and chaotic motions exhibited by the given dynamical system. The method is as follows,

1. First form a suitable oriented surface in phase space (eg. - Blue region in Fig. 2.2).
2. The iterates of the map are given by the points where the trajectory intersects the surface in a specified direction (eg. - From below in Fig. 2.2)
3. The plot of x_{n+1} versus x_n is referred to as the first return map of the system dynamics.

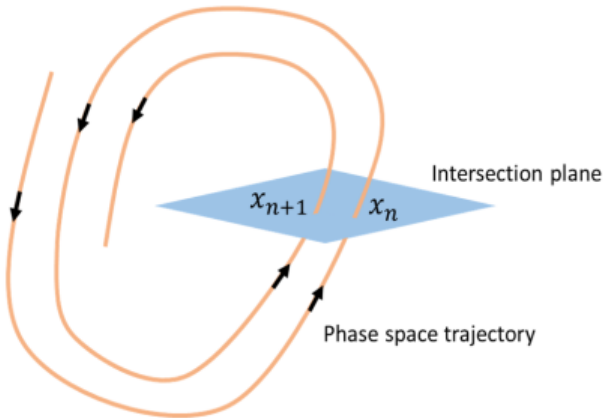


Fig. 2.2 Schematic of Poincaré map formation from phase space trajectory. ([Juniper and Sujith, 2017](#))

In case of a periodic system Poincaré map shows a single point, for phase locked state it shows a set of discrete points scattered around line, while for quasi-periodic system it

shows a closed dense circle in two-dimensional subspace. The Poincaré sections of chaotic or higher-dimensional quasi-periodic systems do not exhibit a simple geometric pattern. If the Poincaré section does not show any of above, the underlying dynamics could be considered as chaotic.

2.3.5 Recurrence Plot

Recurrence refers to the phenomenon of the phase space trajectory revisiting the neighborhood of its previous location, after a time of divergence in the phase space. It is a property of deterministic dynamical systems. With the use of this property, the time evolution of the system dynamics can be qualitatively captured by plotting the recurrence plot (RP). Recurrence plots help in depicting certain aspects of a higher-dimensional attractor into a two-dimensional subspace. The main advantage of recurrence plots is that they provide useful information even for short and non-stationary data.

1. First step to construct RP is to construct phase space using Taken's theorem of delay vectors (Discussed in section 2.3.1).
2. Important parameter required is cut-off threshold. The size of threshold depends on the type of the problem. The increase in the size of threshold results in increase in the number of recurrences in RP.
3. The equation used in constructing RP is

$$R_{i,j} = \theta(\varepsilon - \|\vec{x}_i - \vec{x}_j\|); \quad i, j = 1, 2, 3, \dots, N - (d - 1)\tau \quad (2.21)$$

Where

- \vec{x}_i and \vec{x}_j are the state space vectors.
- ε is predefined cut-off threshold
- θ is Heaviside function.
- N is total number of data points in time series, d is optimum embedding dimension and τ is optimum time lag.

Whenever the phase trajectory falls within the threshold, that is marked as 1 in recurrence matrix; otherwise it is marked as a zero. So the RP becomes a graphical representation

of black and white points, where black points correspond to $R_{i,j} = 0$ and a white point correspond to $R_{i,j} = 1$.

Characteristics of patterns in RP

The structural patterns present in the recurrence plots characterize the dynamical behavior of the phase space trajectory of a given system.

- The diagonal lines in RP depict that trajectories are running parallel to each other.
- The long continuous lines parallel to the main diagonal line illustrate the presence of periodic process, in which the distance between diagonal lines is equal to the period of the system represented.
- Homogeneously distributed black points in the RP indicate a white noise (random) process.
- For quasi-periodic oscillations, RP shows diagonal lines with irregular spacing, manifesting the irrational relation of the instability frequencies.
- In the case of chaotic oscillations, RP depicts the broken short diagonal lines as the neighboring trajectories diverges after a short time of closeness in phase space.
- The vertical lines in RP demonstrate the recurrence (or trapping) of more than one point of the same trajectory inside the predefined threshold.
- The parallel lines orthogonal to the main diagonal line indicate the insufficient embedding of attractor in the phase space.

Chapter 3

Experimental Methods

This chapter discusses common experimental details related to the scope of this project such as setup for acoustic signal, flow control and supply, minimizing the flame disturbance, measurement diagnostics, optical flow visualization techniques, image processing method used for obtaining time series data from schlieren frames, etc.

3.1 Experimental setup

The schematic of experimental setup is shown in Fig. 3.1. The settling chamber made of stainless steel has a layer of honeycomb structure and a wire mesh screens for conditioning the flow, making the flow uniform before it encounters the nozzle. The nozzle can be mounted at the end of the settling chamber. The nozzles used in current experiment are of AR= 1,2,3 with semi minor axis = 1.5 mm. Methane cylinder was equipped with a safety check valve and a pressure regulator through which the absolute pressure upstream of the settling chamber was set for all the experimental runs.

A transparent enclosure of dimension 1700(h) x 600(w) x 600(l) was designed and manufactured in order to reduce disturbances to the flame from surroundings. The air inlets at bottom of enclosure were fitted with wire mesh in order to straighten the incoming air flow. Two sides of the enclosure were fitted with optical window for optical flow visualization purpose. Experimental trial were carried out with and without the enclosure and it was found that without the enclosure also the flame was stable so further experiments were carried out without enclosure.

3.1.1 Data Acquisition - DAQ

All the experiments were monitored and controlled through National Instruments LabVIEW software. National Instruments made PXIe-1078 chassis was equipped with the PXI-8820 embedded controller. A multifunction DAQ device PXIe-6366 was also mounted on the chassis. To facilitate the BNC connections, a shielded connector block (NI BNC-2110) was connected with the DAQ which functions as an extended connector. Flow meter was connected to AI-0 port using BNC connector while PFI-0 pin was used to send trigger signals to Phantom high speed camera which records the high-speed schlieren images. The data was recorded simultaneously from both the high-speed camera and also from the flow controller using a labVIEW codes developed by Mr. Arun B. Nair, PhD student in Aerospace department.

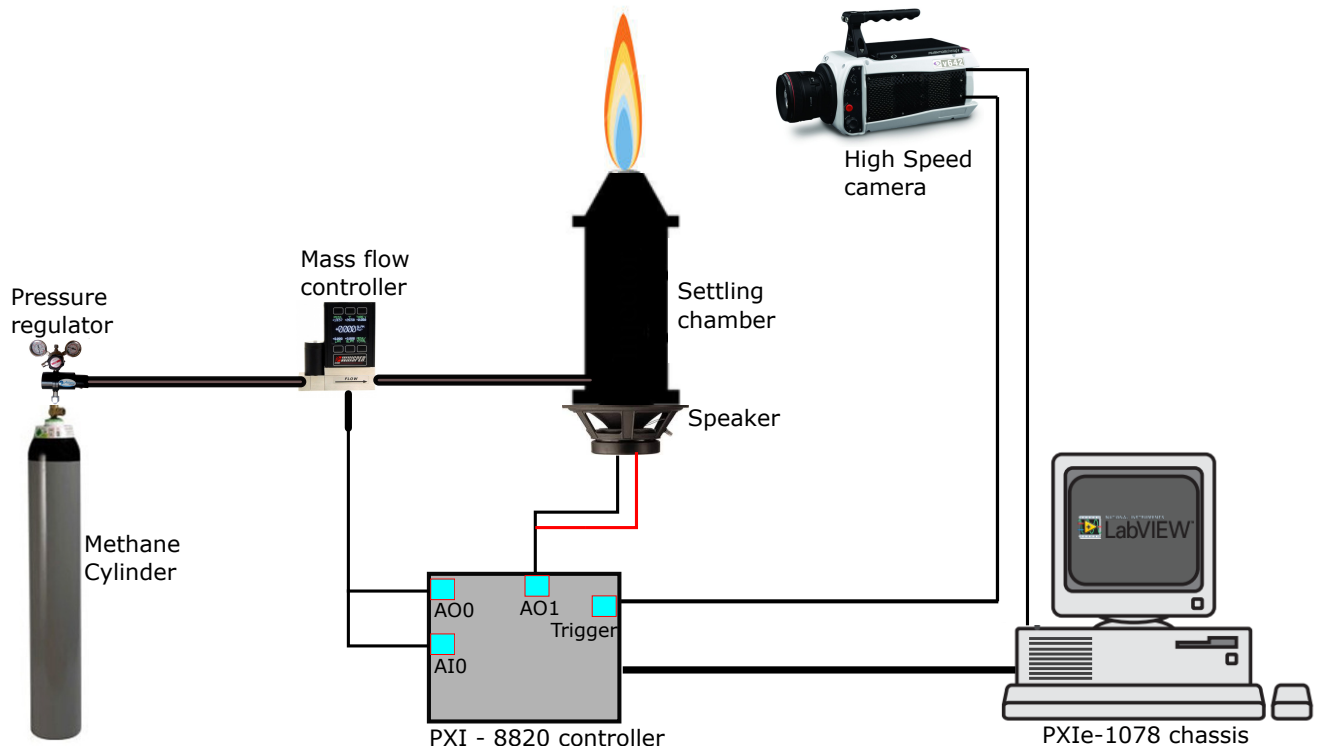


Fig. 3.1 Schematic of the experimental setup.

3.1.2 Flow supply and acoustic system

The flow rates of fuel was measured and controlled by Alicat Gas Mass flow controllers with SLPM range 0-1 and 0-10 (MCS series) according to the requirement of the experiment. It provide an accuracy of \pm (0.8 % of reading + 0.2 % of full scale) . The flow controller was

given Analog input from National Instrument PXI-8820 controller which was controlled by a program written in labview as explained in section 3.1.1, the time-series data of the fuel flow through controller was also recorded throughout each experiment to have a check and control on the flow fluctuation during the experiment run. Flow Temperature and pressure were also recorder from the mass flow controller before start of each experiment to make sure that the experimental conditions does not deviate much from the standard laboratory conditions.

Acoustic excitation to the fuel was achieved by fixing a speaker at the bottom of the settling chamber. The speaker used was a **3 inch midrange woofer** from Aura Sound. For particular specifications the reader is encouraged to look at the user manual of speaker. The frequency and amplitude input to the speaker was provided by the same DAQ using labview program. The acoustic input signal verification was done using a oscilloscope. The speaker input signal supplied by labview program was also compared with a signal from a signal generator and it was found that the signal generated by labview program was much better in terms of noise in signal at lower frequency and amplitude and hence was used for all the experiments involving acoustic excitation.

3.2 Optical flow visualization

Optical flow visualization methods are based on changes of fluid density; hence its index of refraction. As a result of these changes, optical phase and, coupled with it, direction of propagation of a light wave transmitted through the flow are altered in comparison to the properties of the incident light. The available signal can be presented in planar form, i. e., as a flow picture.

Three popular optical flow visualization methods are Shadowgraph, Schlieren and Interferometry. These are listed in order of increasing complexity and possible variations. The flow visualization method chosen for scope of this experiment was schlieren because of problem encountered in other techniques caused by high intensity of flame, which is a self-luminous object and was causing our data to get saturated. Schlieren setup is actually nothing more than Shadowgraphs in which the deflected rays are interfered with in some manner, rather than allowing these rays to reach the imaging screen undisturbed.

3.2.1 Schlieren Visualization

Schlieren is sensitive to change in first derivative of gas density. It should be noted that the schlieren used for this setup is not a method suitable for direct quantitative measurement of

density. However the method is convenient for qualitative analysis of flow fields with varying density.

Among different types of schlieren setups¹ "Z" type with mirrors is most popular and preferred because of

- Mirrors are free from chromatic aberration, which in case of lenses causes the focal length to be variable based on the wavelength of light passing through the lens and hence in case of schlieren visualization the location of knife edge varies with each color.
- Mirrors have the added advantage over lenses that they need to only have one surface ground and polished and that defects in the substrate are usually of much less significance. Thus mirrors are less expensive and much better than lenses.
- Distance between mirrors can be adjusted even for large test-sections.

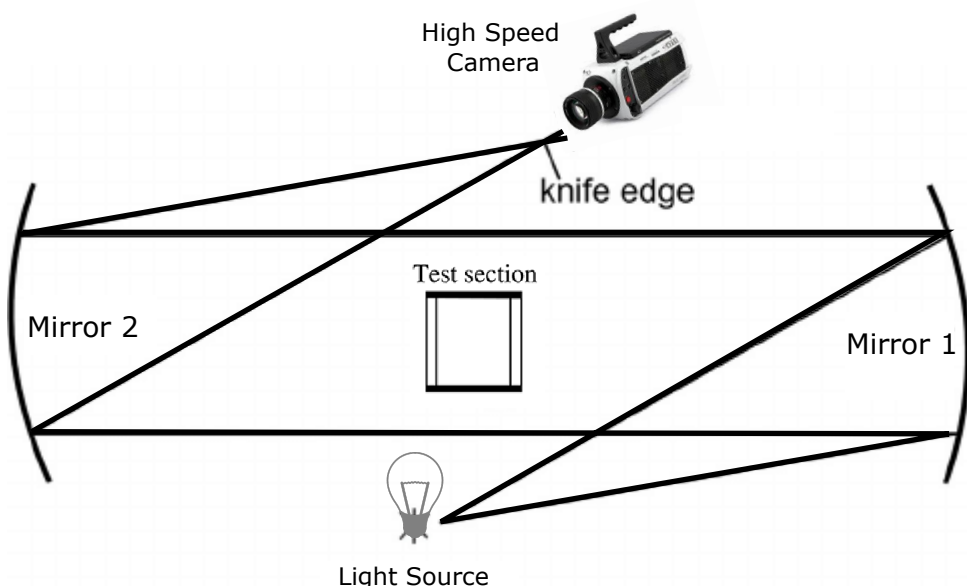


Fig. 3.2 Schematic of Z type schlieren setup.

In this as shown in Fig. 3.2 the light source is located to one side of one of the two schlieren mirrors and exactly one focal length away from the mirror. Because of it's placement in this position, the mirror projects a more or less parallel beam of light, as if trying to focus the light from the source at infinity. The location of the source, in fact, is adjusted until the emerging beam from the mirror maintains the same diameter over an extended distance.

¹A review of recent development in schlieren is provided in [Settles and Hargather \(2017\)](#)

A second mirror, which can be located a considerable distance from the first, thus allowing the test section to be placed between them, intercepts the light beam from the first mirror. Because it is parallel and therefore appearing to come from infinity, the second mirror brings this light to a focus, and forms an image of the source one focal length from its surface. The mirror is turned so that it places the image on the opposite side of the beam as the location of the source. This placement tends to reduce aberrations introduced by the first lens being at an angle to the source.

The purpose of knife edge at the focus of second mirror is to cause gradual overall darkening which helps in reducing the overall brightness. Being exact at the focus of second mirror, knife edge cuts into the beam of light coming from the surface of 2nd mirror which results in a fewer light rays reaching the camera lens and hence the corresponding image point on screen, thus causing the brightness to fall. The same effect can also be achieved by reducing the size of the light source itself.

In order to be able to record a schlieren of reduced size with a camera, the recording plane (photographic film, chip of an electronic camera) is focused by means of the camera lens onto the plane at a distance l from the object. In this way, the object is not in focus in the schlieren picture, which helps in reducing the radial influence of self-luminous object.². A detailed information about optical flow visualization techniques is mentioned in [Davidhazy \(2006\)](#) and [Settles \(2001\)](#)

Table 3.1 Details about schlieren optical setup components

Light source	LED
Mirror focal length	120.4 cm
Mirror diameter	12 inch
Camera	Phantom high speed camera

3.3 Image Processing

For analysis of the time series data of the flame, the intensity in each frame of each video is summed across every pixel column (w), generating a time series at each axial location: $I(x/D_{minor})$. The codes for generating time series data from frames were written in MATLAB.

²A spatial filtering technique for reducing radial influence of self-luminous is explained in [Zhu et al. \(2016\)](#)

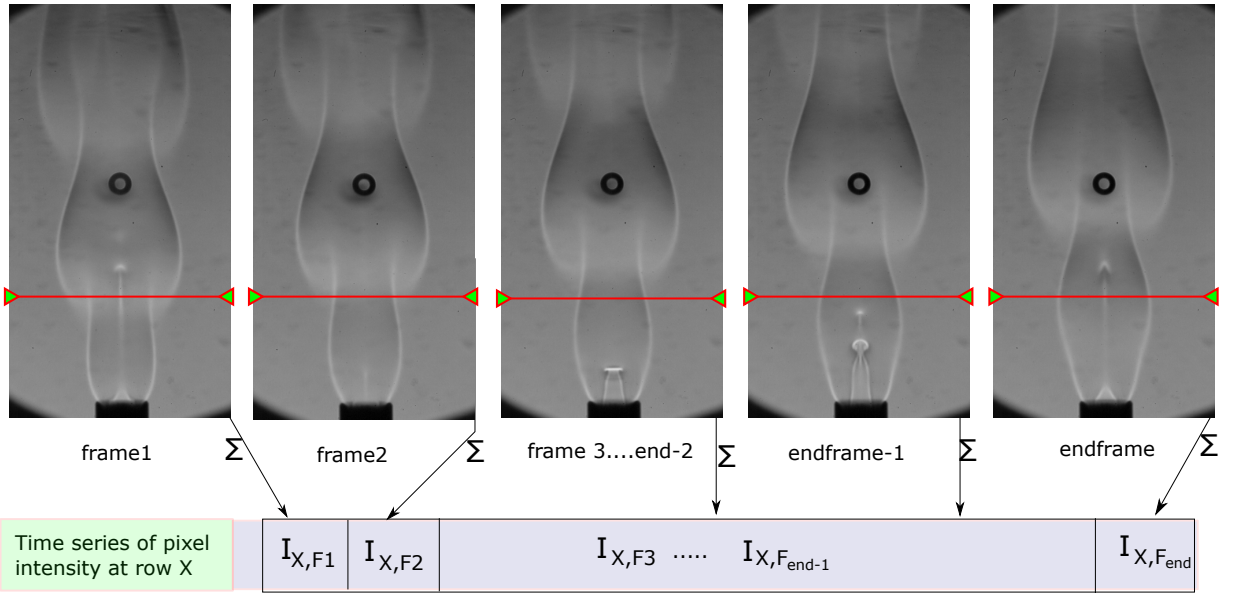


Fig. 3.3 Representation of procedure to obtain time series data of schlieren emission at $x/D = 10$ location. The same procedure is applied to any other location needed for analysis.

Figure 3.3 illustrates the procedure followed in image processing in order to obtain time series data from frames. For most of the analysis a location with $x/D = 10$ was selected mainly because of three reasons

1. It is sufficiently far downstream that the chemiluminescent or schlieren emission leads to a reliable signal-to-noise ratio without saturation.
2. It is sufficiently far downstream that the global mode has time to grow and interact with the forcing
3. It is not so far downstream that it coincides with the location of vortex roll-up, where the strain rates can be high enough to cause local flame extinction, especially if high forcing amplitudes are used.

Further analysis which includes local and global decomposition analysis, non-linear time series analysis are done to understand the rich information about the flow physics hidden in time series.

3.4 Precautions implemented during experiment

1. All the connections were leakage tested with compressed air at 2 bar pressure using soap bubble test.

2. All the running fans, exhausts systems were turned to quite mode before running a experiment and a relaxation time of 5-10 minutes were given for stabilization of circulation of air in the laboratory.
3. Ensured the minor/major side of the ellipse nozzle is properly aligned with the parallel light beam when acquiring the schlieren images.
4. The schlieren setup alignment was checked regularly and ensured that the knife edge was placed at the focus of mirror.
5. Before start of each experiment run it was ensured that the surrounding conditions do not deviate much from the standard laboratory conditions.

Chapter 4

Natural Characteristics of Circular and Elliptic Diffusion Flame

In this chapter the results of the experiments performed to understand natural flickering behavior of circular and elliptic diffusion flames with varying velocity/flow rate are discussed. A total of three nozzles which includes one circular and two elliptic nozzle with AR = 2,3 are studied experimentally. The starting point of flow rate range is decided based on the onset of buoyant flickering for nozzle and the end point is decided based on the disappearance of the buoyant flickering behavior as we increase the flow rate (Fig. 4.1).

The experiments are performed with 99.5 % pure methane gas and their response is measured using a high speed camera via schlieren optical flow visualization technique. The camera settings used for current set are included in Table 4.1.

Table 4.1 Camera settings used to capture natural oscillations schlieren imaging

Frame rate	180 frames s^{-1}
Exposure time	10-300 μs
Resolution	384(w) x 800(h) and 128(w) x 512(h)
Field of view	44.64 D_{minor}
Image Type	8 bit monochrome
Image Scale	5.7714 pixel per mm
Video length	5883 frames
Post trigger	5883 frames
Auto exposure	Off

* D_{minor} is equal to the minor axis length for elliptical nozzles which in current study is same as 3 mm for all nozzles. Reynolds number is calculated based on the equivalent diameter of circular nozzle which has same area as of elliptic nozzles, which comes to be

$$D_{eq} = 2\sqrt{ab}$$

$$Re = \frac{\rho * V * D_{eq}}{\mu}$$

Where a is semi major axis, b is semi minor axis of the ellipse and V is the velocity of fuel at nozzle exit. Unless mentioned otherwise the Reynolds number throughout this thesis is calculated as mentioned above.

4.1 General Characteristics

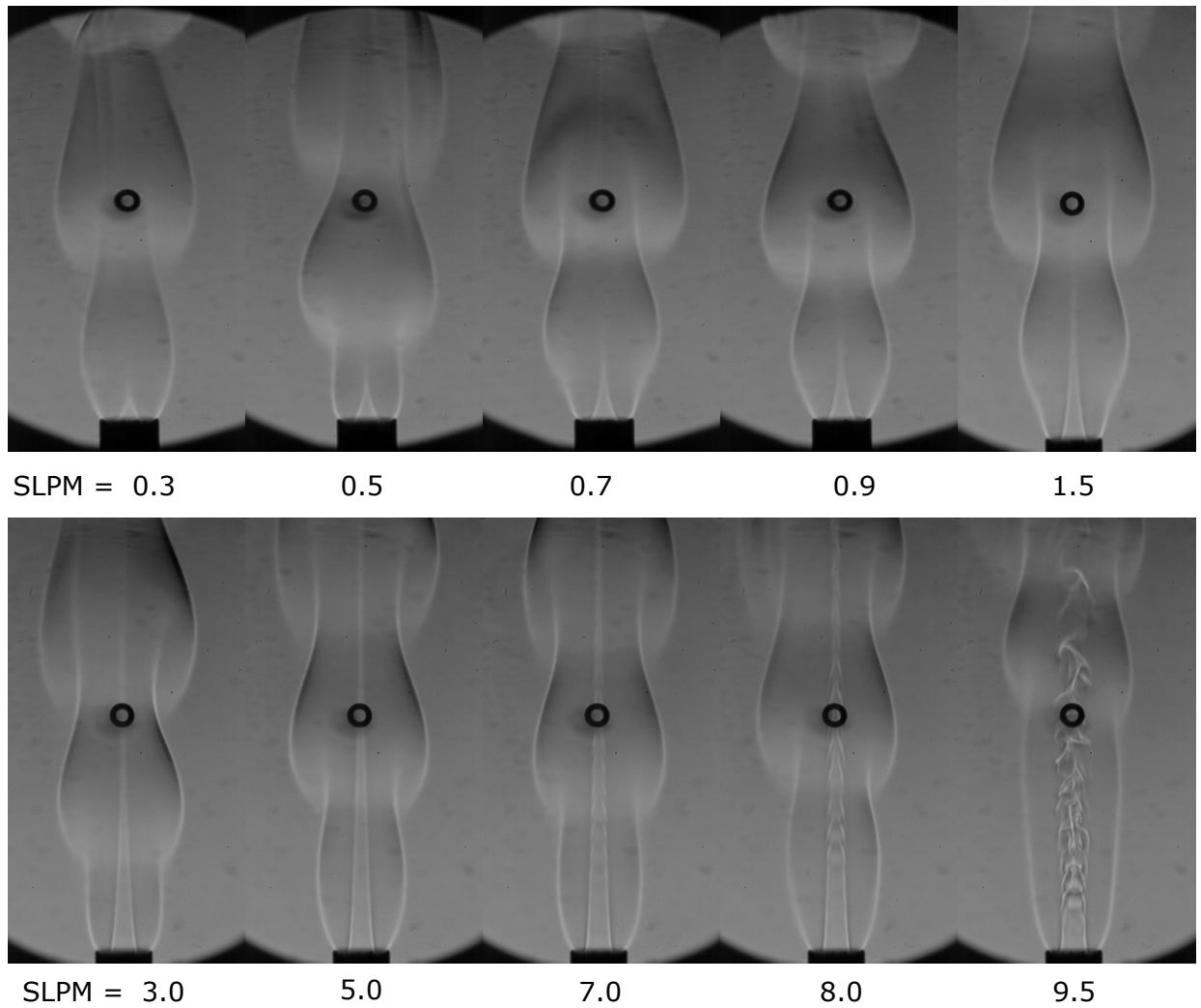
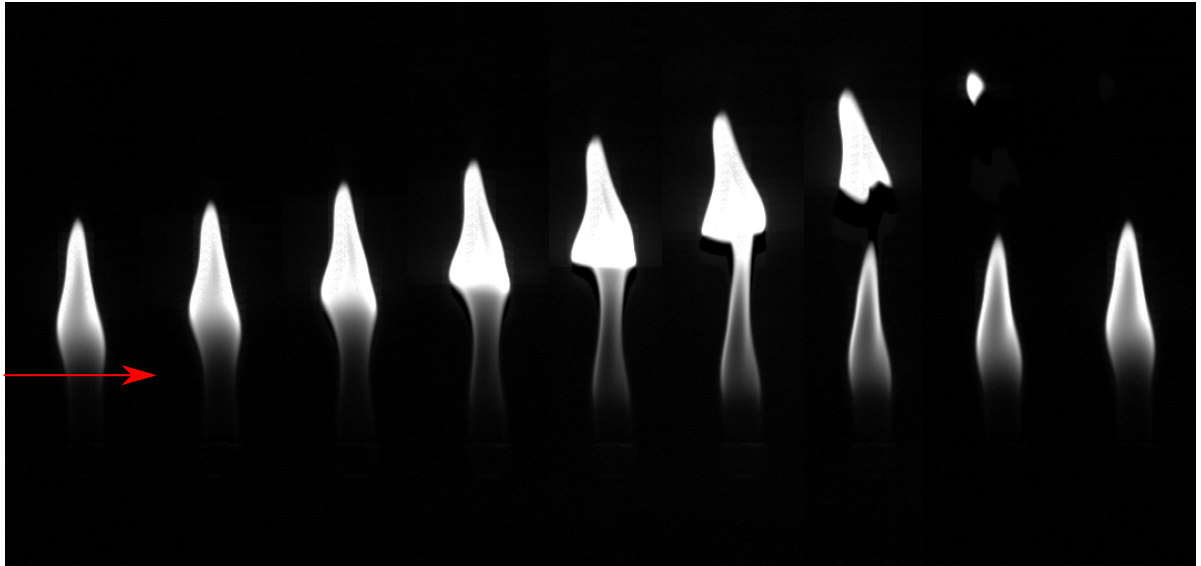
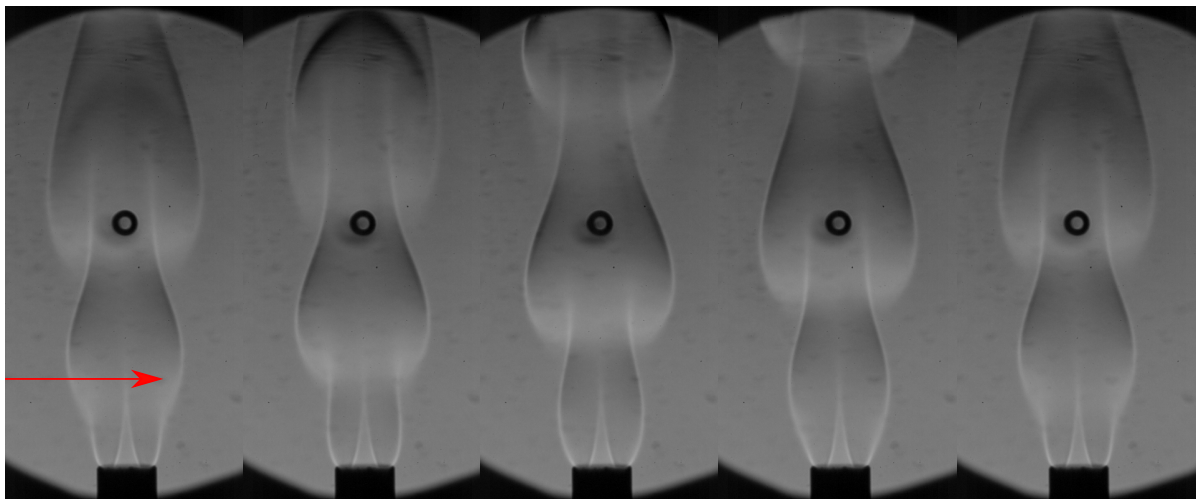


Fig. 4.1 Variation of schlieren flow field with flow rate for AR = 3 elliptic flame.



Direct Chemiluminescence Visualization



Schlieren Visualization

Fig. 4.2 Image sequence of natural oscillations as seen from major axis side for flame with $AR = 3$ elliptic nozzle at flow rate of 0.9 SLPM ($Re = 219.53$), which has natural oscillation frequency = 11.26 Hz. The sequence runs from left to right, and the images are separated by 1/8 and 1/4 of time period of global oscillations in direct and schlieren visualization respectively. The red arrow indicates the location $x/D = 10$ at which time-series data was extracted for further analysis.

Figure 4.1 shows the variation schlieren flow field for $AR = 3$ elliptic nozzle flame. At $SLPM = 0.3$ the flame starts showing buoyancy induced oscillations and the length of the center jet increases as the flow rate increases. The flame shows varicose mode of oscillations as can be seen from the symmetry of flame/vortices structure. The vortices size

also increases with flow rate and the origin point of vortices starts to shift upstream of nozzle. At SLPM = 7.0 the flame center jet structure starts to show meandering and the buoyancy dominated vortices only exist very upstream of nozzle. Further increasing the flow rate causes turbulence at the tip of flame causing the buoyancy oscillations to disappear. Turbulence travels downstream the flame and the center jet meandering also becomes turbulent and distorted. Similar flow field structures were seen in circular and AR = 2 elliptic flame, when seen from major as well as minor side.

Table 4.2 Experimental parameter for natural oscillations study

Nozzle	Sets	Re	Fr	No. of experiments
Circular	11	100 - 1700	1 - 3100	22
Elliptic AR = 2	12	50 - 1100	1 - 1200	48
Elliptic AR = 3	14	40 - 950	1 - 550	56

4.2 Unsteady characteristics of flame

Local decomposition techniques like Fourier Transform, Spectrogram are methods which can only be applied to time series of data obtained at a point of interest in domain. The results obtained for flame with AR = 2 elliptic nozzle with flow rate = 0.8 SLPM (velocity = 0.9431 m/sec) are discussed here because of brevity. The same analysis was carried out for each experiment set in order to understand the different characteristics of flow field with time at any point within the domain of interest.

4.2.1 Temporal variation of flickering frequency

Figure 4.3 shows power spectrum of time series signal and it is clearly observable that only 11.73 Hz and its super-harmonics are present in spectrum indicating that the natural varicose oscillation is not perfectly sinusoidal and also concludes that the flame flickers with its natural oscillations frequency = 11.73 Hz.

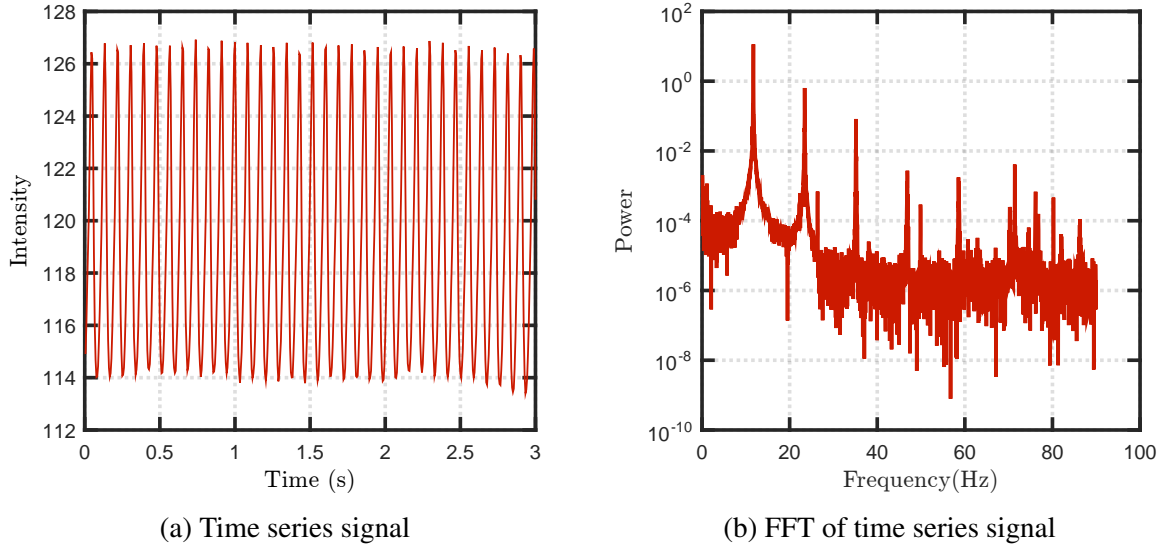


Fig. 4.3 (a) Time series signal and (b) FFT of time series signal obtained at $x/D = 10$ for AR=2 elliptic nozzle with $Re = 239$.

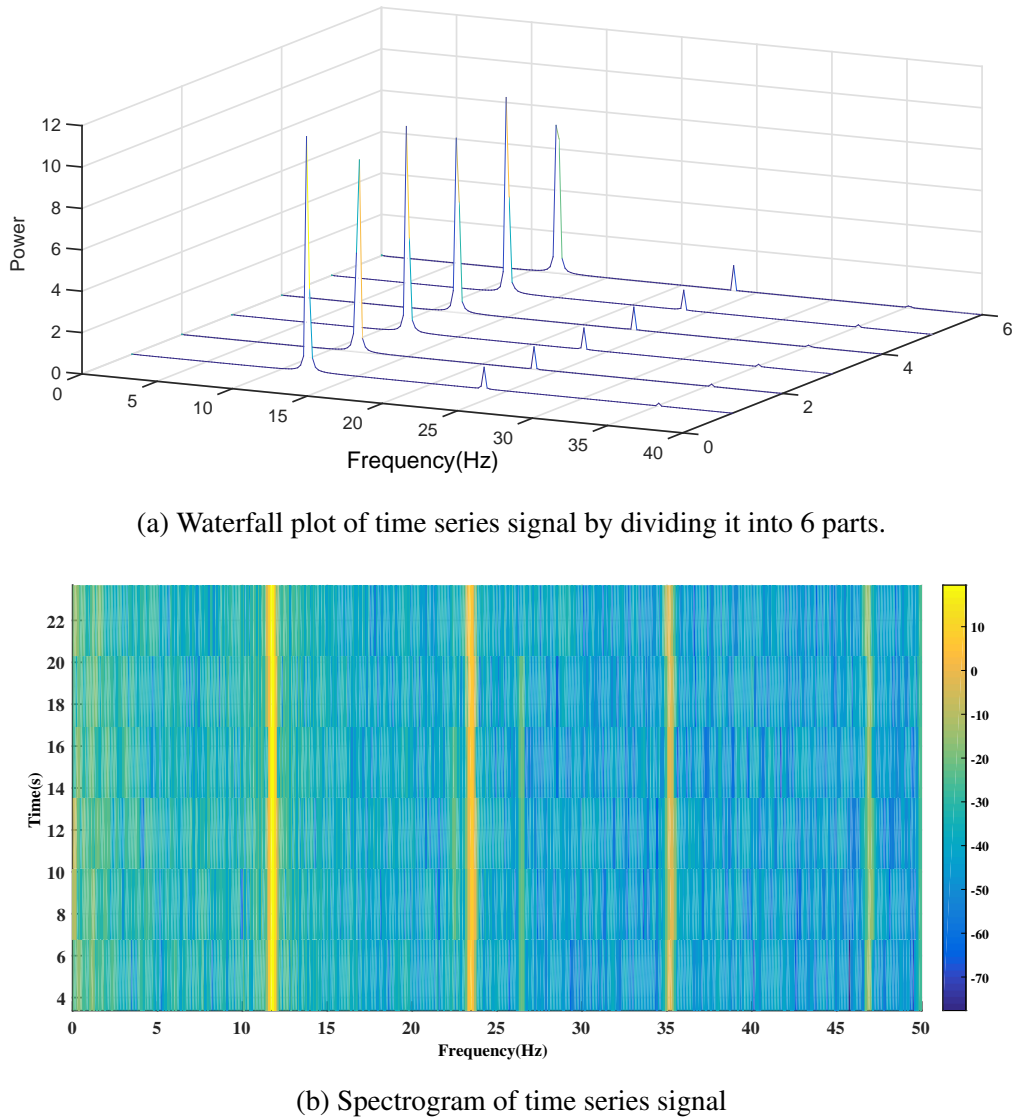


Fig. 4.4 Waterfall and Spectrogram plots for AR = 2, $Re = 239$, natural oscillations case.

FFT analysis is not useful in case the signal is non-stationary because the time information is lost in Fourier Transform. Figure 4.4a and 4.4b shows waterfall and spectrogram plots which helps in understanding the frequency present in signal with respect to time. Both Fig. 4.4a and Fig. 4.4b shows a single frequency dominance and its super-harmonics presence in signal with time which means time series signal is stationary and the flickering frequency of flame does not vary with time.

4.2.2 Spatial variation of flickering frequency

Last subsection discussed about flickering frequency at point $x/D = 10$ and its variation with time, but for this to be called a global flickering frequency for the flame the same frequency dominance has to be seen throughout the domain of interest. To understand this the time series signal and its FFT is plotted for different x/D ratios starting from near the nozzle, moving downstream of the flame toward the tip. For current resolution setting the field of view is limited to 44.64 times D_{minor} (table 4.1), and hence the max x/D selected is 40.

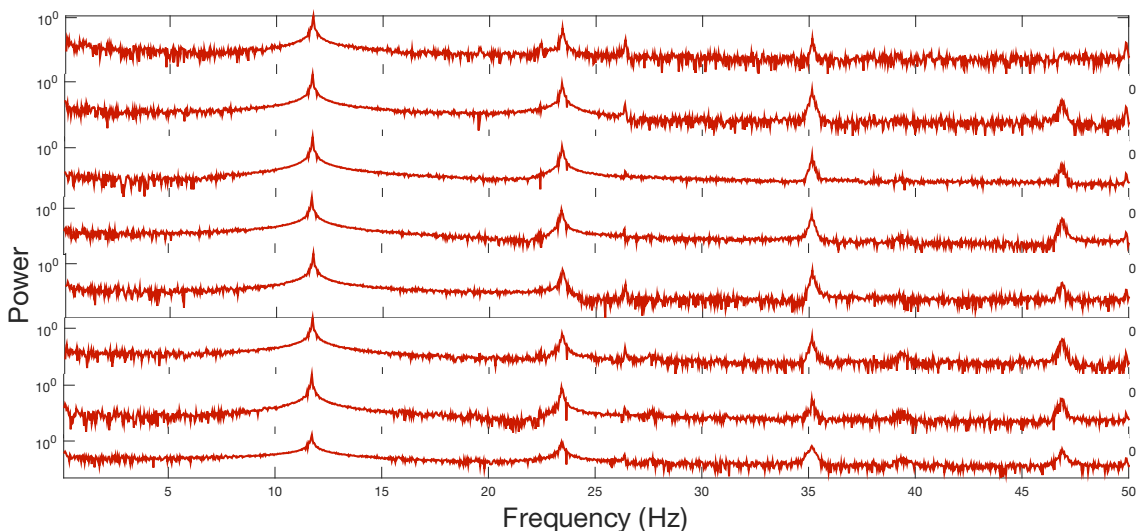
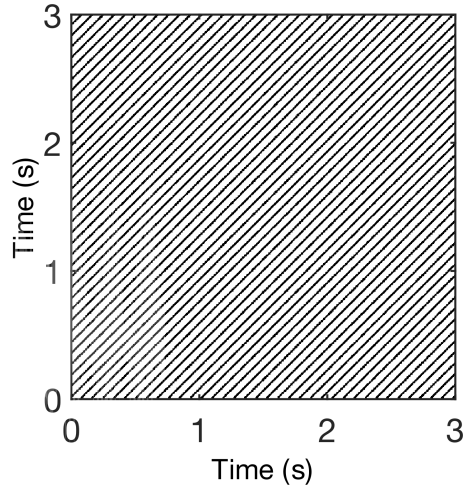


Fig. 4.5 Power spectrum plot of signal at $x/D = [5, 10, 15, 20, 25, 30, 35, 40]$ locations. The sequence moves from bottom to top. The spectrum peaks are at frequency = 11.73 Hz and its super-harmonics.

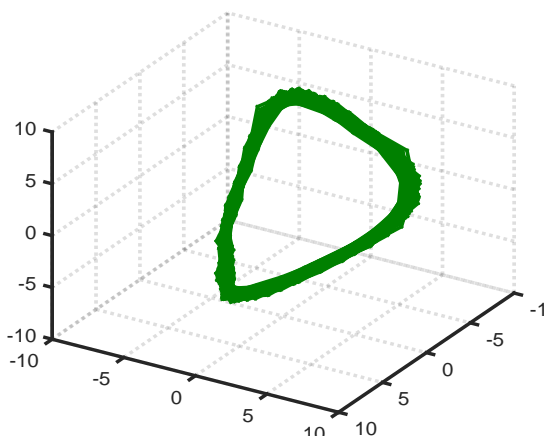
It can be clearly seen in the Fig. 4.5 that the peak in power spectrum is at the same frequency in all x/D locations. The same analysis was done (not shown) for schlieren data obtained as seen from minor axis side at all x/D location for the same flame with same flow conditions and the frequency was found to be same, which means that flickering frequency is indeed **global** in nature for the flame.

4.3 Results from non-linear time series analysis

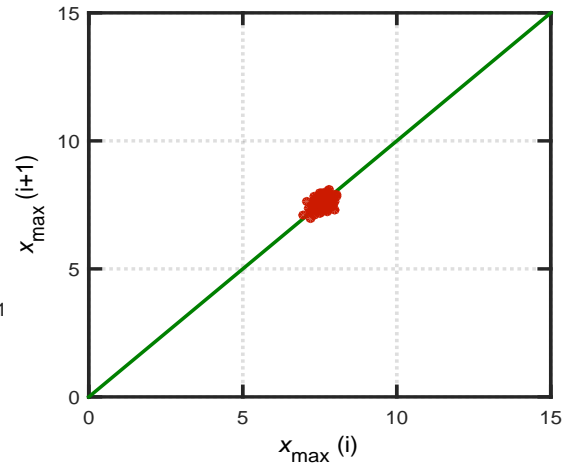
Analysis using non-linear time series analysis tools for a flame with AR = 2 elliptic nozzle, Re = 239 (flow rate = 0.8 SLPM) is discussed in this section. As discussed earlier this flame shows natural **global** oscillations with frequency = 11.73 Hz.



(a) Recurrence plot



(b) 3D phase portrait



(c) Poincaré map

Fig. 4.6 Non-linear time series analysis plots for AR=2, Re = 239, major side case.

Figure 4.6b shows phase space constructed by Taken's method of delay vectors (Section 2.3.1) and it shows a limit cycle which indicates periodic oscillations in the signal. Theoretically the limit cycle curve should be single closed curve in 3D phase portrait and the poincare map should show only a point but because of presence of some noise in experiments

the trajectory is not perfectly closed and it looks like a cluster of points scattered around one blob in return map. The recurrence plot shows equally spaced diagonal lines which is also an indicator of periodic oscillations with time period equal to the spacing between the diagonal lines.

4.4 Results from DMD

DMD was done on schlieren snapshot to understand different dynamic modes of the flame. DMD gives us spatial characteristics of a mode which has a unique frequency. As we have seen that flame oscillations are global and periodic in nature, DMD will help us understand modes corresponding to that global frequency.

Dynamic mode decomposition was done for same case (AR=2 nozzle, Re =239, Major axis side) by using 2000 frames (recorded at an fps of 180) from that dataset of 5883 frames. The cross section selected for DMD analysis is shown in Fig. 4.7

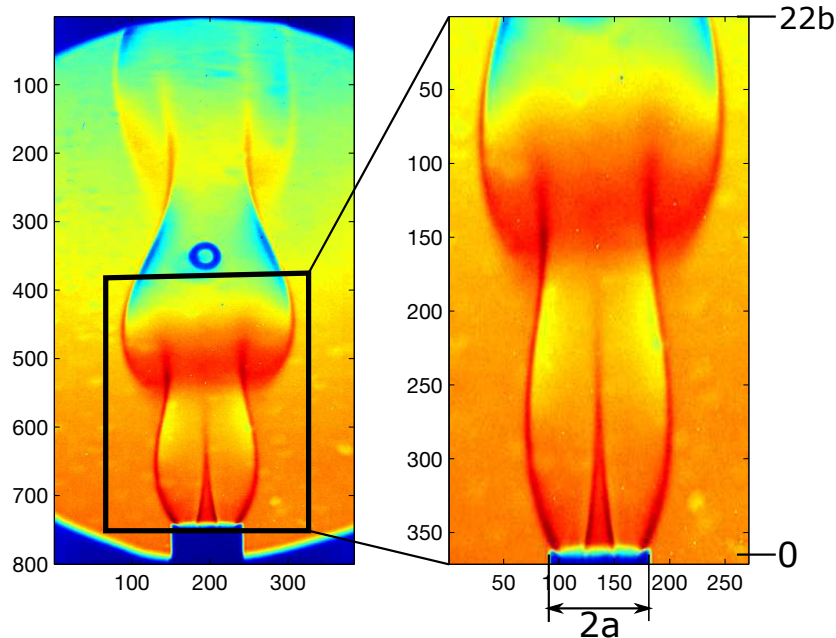


Fig. 4.7 (a) Actual flow field snapshot and (b) region of the field selected for DMD analysis.

Figure 4.8 shows DMD spectrum and eigenvalue distribution for current analysis. As mentioned earlier in text, eigenvalues are related to temporal characteristics of the dynamic modes and in saturated oscillations most of these are concentrated around the unit circle, since growth rate is defined as real part of $\log(\lambda)/\Delta t$, the modes which lie on unit circle has

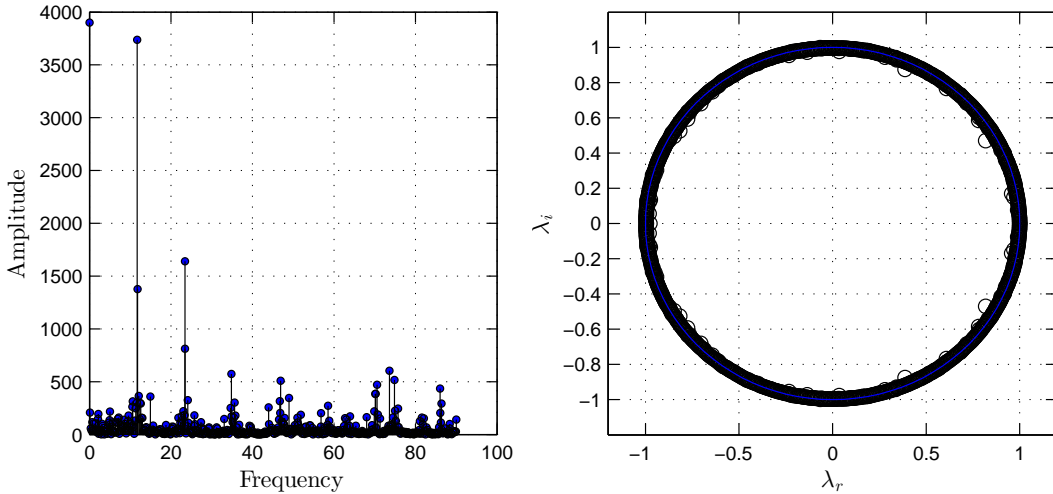


Fig. 4.8 (a) DMD spectrum and (b) Eigenvalue visualization for flame with AR = 2 nozzle, Re = 239, major side visualization.

zero growth rate while modes which are inside has negative growth rate and they will decay with time but if the point lies outside the circle which will mean that the mode is growing.

For current analysis most of the DMD eigenvalues are on the unit circle so it can be said from the Fig. 4.8b that amplitude of oscillation has been saturated. Fig. 4.8a shows amplitude of modes with respect to corresponding frequency, the selected dominant modes are further processed to obtain spatial features of these modes.

Figure 4.9 shows spacial characteristics of mean mode (Frequency = 0), dynamic mode 1 (frequency = 11.71 Hz)¹ and mode 2 (frequency = 23.42 Hz). Since the dynamic modes are formed form eigenvectors of A they have both real and imaginary part and a unique frequency associated with each mode. Given that our experimental data is real, reconstruction of dynamics should be done using real part only but the imaginary part of modes tell us important information when we see the phase information of modes. Magnitude of the modes help us see what are the regions of importance with respect to that mode and tells us what spatial regions are active with respect to which modes.

First mode is mean mode, having zero frequency, its imaginary part has zero intensity everywhere. Looking at the dynamics of different modes we can tell that all 3 modes are symmetric about direction of fuel outlet, but while looking at phase plots of modes we can tell about leads and lags of spatial regions in each mode, for example in case of mean mode the phase plot shows that there is π phase shift in some region as we move downstream of flame there is a asymmetry in direction perpendicular to flow direction which indicates

¹Since resolution of FFT for this case is 0.0395, 11.73 and 11.71 are considered to be same.

that this is the region where vortices are forming, similarly in other modes also the phase difference between different x/D location can be seen. This helps us understand that modes are not only providing magnitude for intensity but also are responsible for formation of vortices structure in flame flickering.

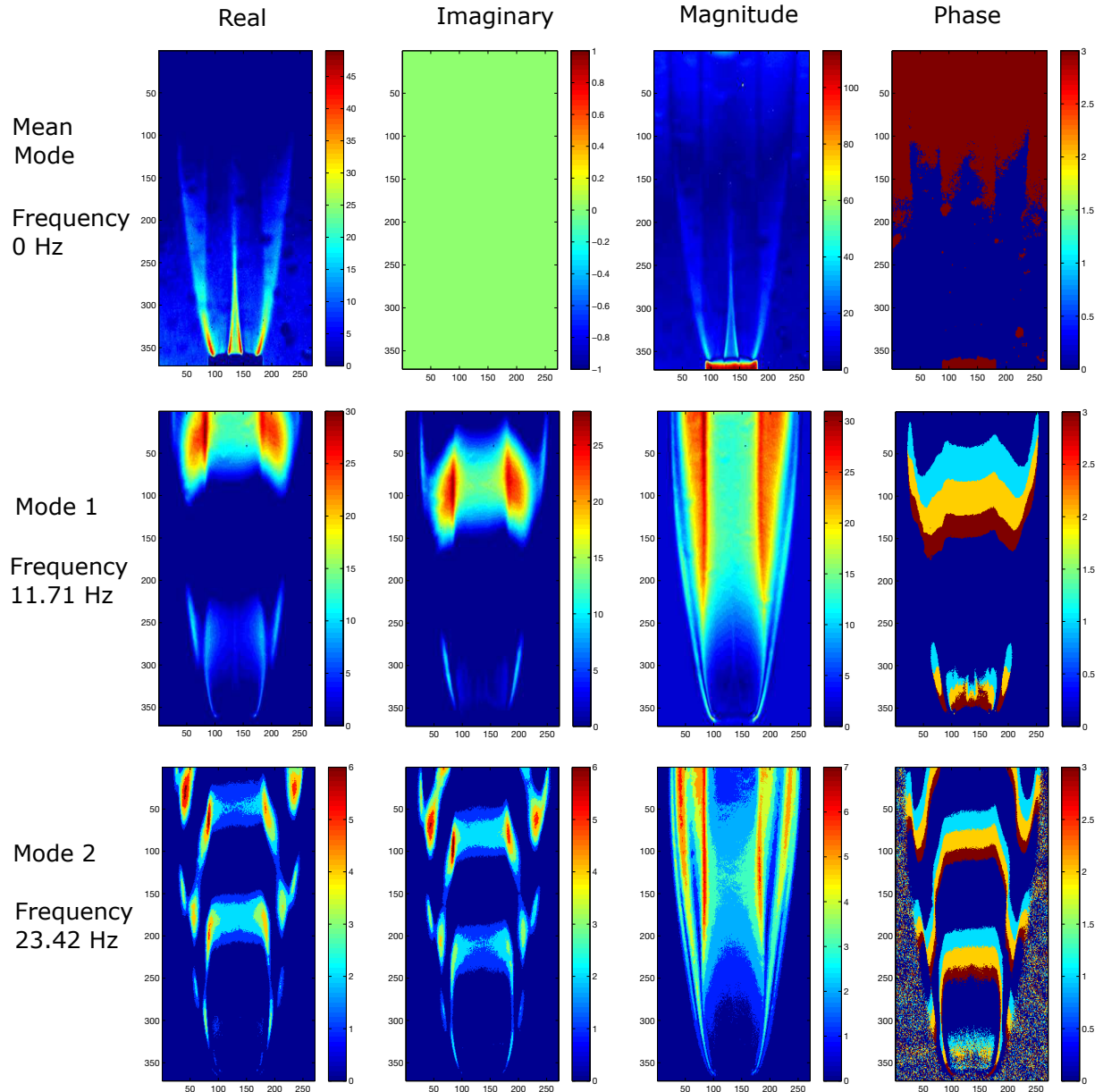


Fig. 4.9 Spatial characteristics of mean and first 2 DMD modes for $AR=2$, $Re = 239$, major axis side case.

4.5 Effect of aspect ratio on flickering frequency

Primary aim of this section is to discuss how does changing the aspect ratio of nozzle changes the correlation between Strouhal number and Froude number. Experiments were carried out for a total of 3 nozzles with AR = 1, 2, 3 with semi-minor axis (b) = 1.5 mm. The starting and end range of flow rate to be considered for all nozzles was decided based on the onset of flickering due to buoyancy and the disappearance of flickering due to turbulence in flame as we increased the fuel flow rate.

The objective is to find a universal scaling (if exist) in terms of characteristic length which affects correlation between Strouhal number (St), and Froude number (Fr), which is the ratio between the inertial force and buoyancy force. They are defined as

$$St = \frac{fD}{V}, Fr = \frac{V^2}{gD} \quad (4.1)$$

where D is the characteristic length, V is the velocity of fuel at the nozzle exit, f is frequency of oscillations and g is acceleration due to gravity.

[Hamins et al. \(1992\)](#) observed that the fuel velocity at the burner exit has a weak influence on the pulsation frequency for some diameters in case of circular nozzles. The Strouhal number plotted as function of the inverse Froude number was also shown to correlate the measurement determined. The correlation between St and Fr was found to be of a power law form.

$$St = K_1(1/Fr)^m \quad (4.2)$$

Similarly between St and Re

$$St = K_2(Re)^n \quad (4.3)$$

Where m and n are the exponents and K_1 and K_2 are the intercepts of power law fit.

From equation 4.1 and 4.2 we can write,

$$f \propto \frac{g^m d^{m-1}}{V^{2m-1}} \quad (4.4)$$

For a constant diameter, deviation of m from 0.5 indicates dependence of frequency on velocity,

- If $m = 0.5$, frequency is independent of velocity.
- If $m > 0.5$, frequency will decrease with increase in velocity.

- If $m < 0.5$, frequency will increase with increase in velocity.

In case of elliptic flame the most common characteristic length chosen is based on equivalent area circular nozzle, i.e., $D = 2\sqrt{ab}$, where a and b are the semi major and semi minor length of nozzle. Figure 4.10 shows experimental data and power law fit for St vs Fr and St vs Fr with $D = 2\sqrt{ab}$ for all three nozzles. Power law fit exponents and intercepts for this case are shown in table 4.3. It can be clearly said that all the three nozzles satisfies different power law relation which means this cannot be used as a universal scaling.

Table 4.3 Power law fit for $D = 2\sqrt{ab}$

nozzle	St vs Fr		St vs Re	
	exponent (m)	Intercept (K_1)	exponent (n)	Intercept (K_2)
Circular or AR = 1	0.4485	0.1726	-0.8970	3.7273
Elliptic AR = 2	0.4650	0.2197	-0.9301	8.6211
Elliptic AR = 3	0.4726	0.2465	-0.9451	13.6765

In order to find a scaling, correlations from experimental data were plotted for a total of three scalings including the one discussed above.

1. $D = 2\sqrt{ab}$

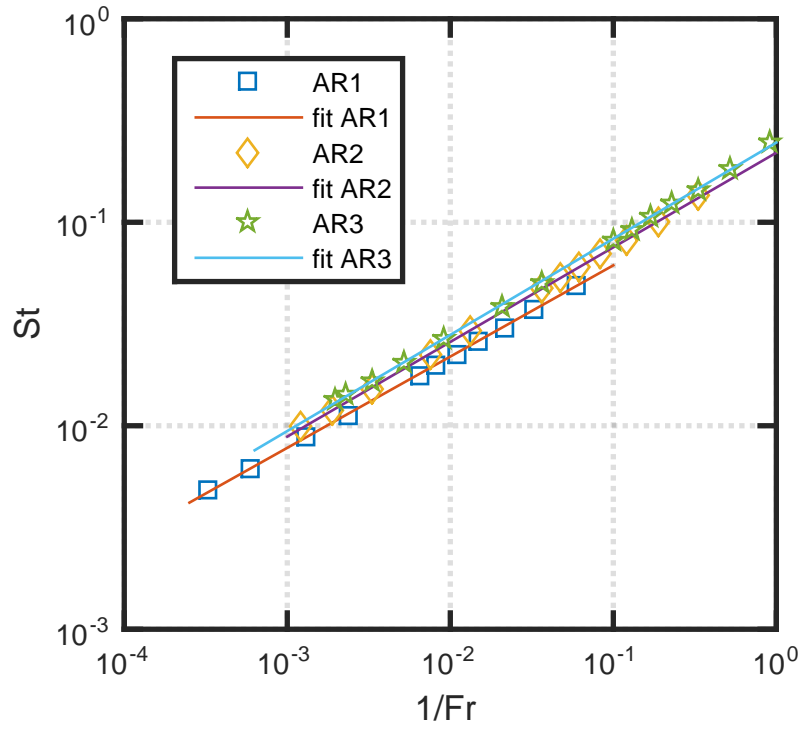
2. $D = 2b$

3. $D = 2a$

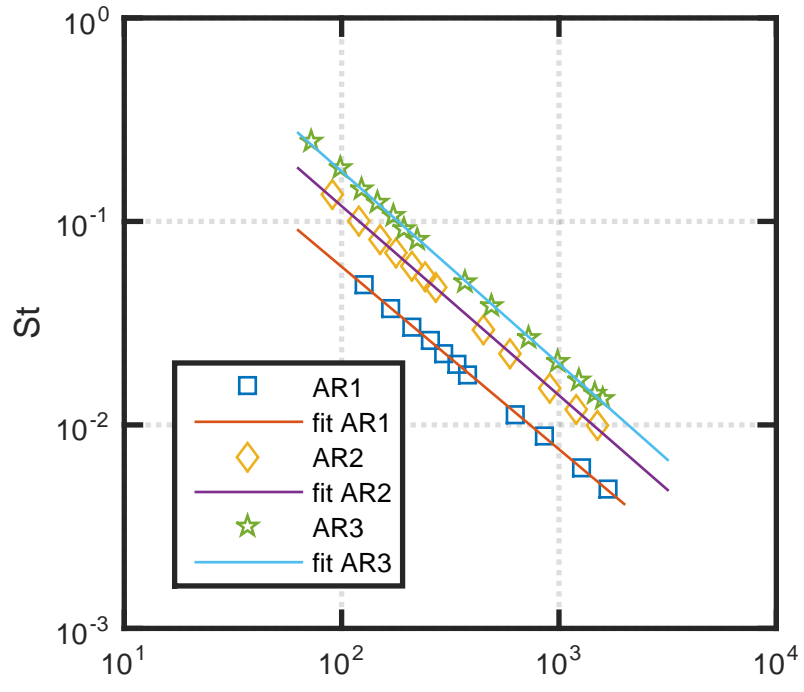
Figure 4.11 and shows experimental data and power law fit for St vs Fr and St vs Fr with $D = 2a$ for all three nozzles. Again this scaling is also not able to capture features of different nozzle under a single correlation ad hence cannot be considered as universal scaling.

When $2b$ was selected as characteristic length (D), experimental data corresponding to all three nozzles follows a single fit within experimental uncertainty. So it can be said that the natural instability in case of diffusion flame is only dependent on minimum distance between shear layers (which is $2b$) and varying the AR does not change the correlation between St and Fr for this scaling. Table 4.5 shows intercepts and exponents for fit in case of $D = 2b$.

It can be seen from the tables 4.4 and table 4.10 that on changing the characteristic length the intercept in power law fit changes while the exponent remains unchanged. The exponent m for AR = 3 nozzle is closest to $m = 0.5$ because of which the dependence of frequency on velocity is much less compared to AR= 1, 2 nozzles. Similarly comparison between AR = 1



(a)



(b)

Fig. 4.10 (a) Strouhal number vs Froude number, (b) Strouhal number vs Reynolds number for natural oscillations in case of $AR = 1, 2, 3$ nozzles. The characteristic length D is $2\sqrt{ab}$.

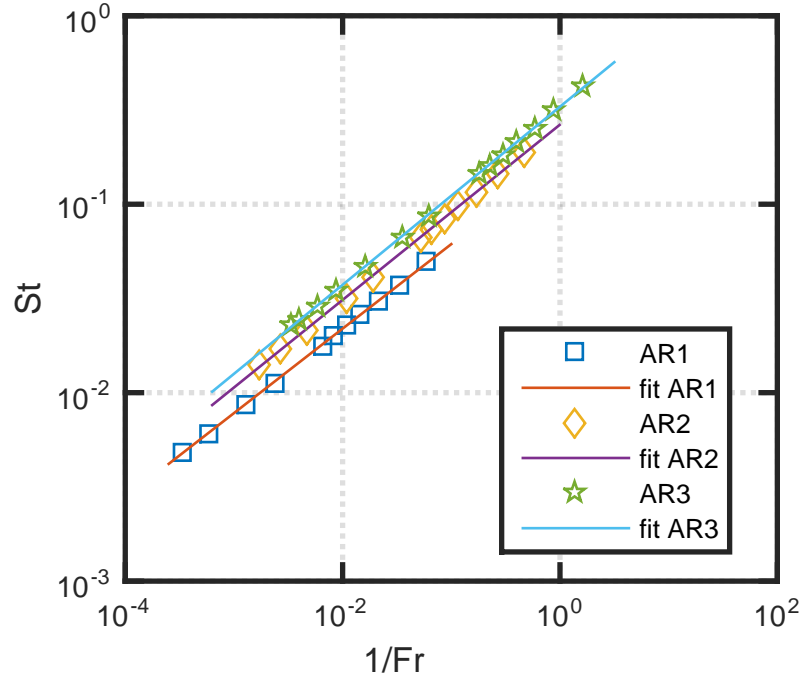
and AR = 2 tells us that the flickering frequency in case of circular nozzle is the most sensitive to change in velocity. All three nozzles have $m < 0.5$ which means the velocity dependence is positive for all nozzles. Similar conclusion about fit between St And Re can also be made but they do not provide any additional information hence they are not discussed here.

Table 4.4 Power law fit for $D = 2a$

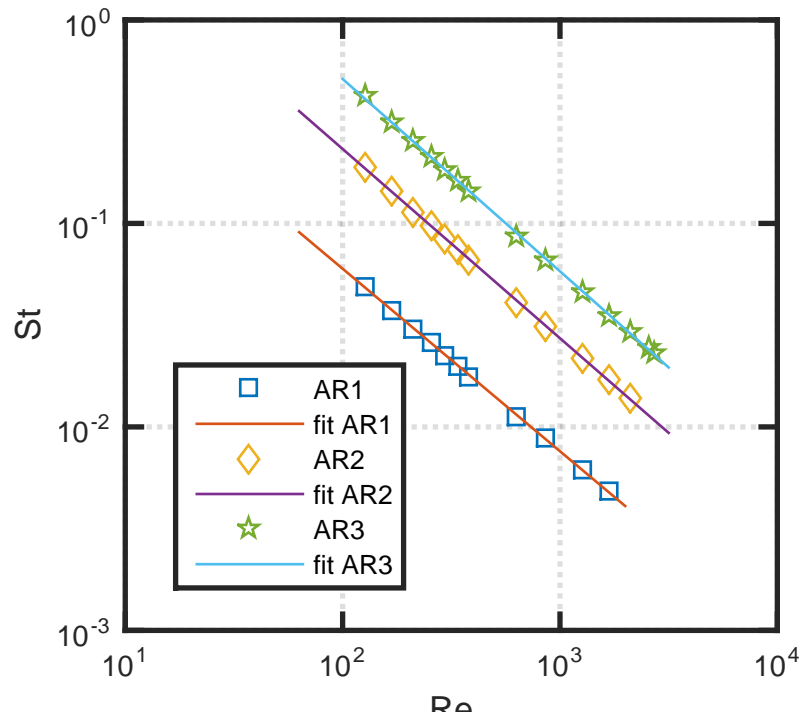
nozzle	St vs Fr		St vs Re	
	exponent (m)	Intercept (K_1)	exponent (n)	Intercept (K_2)
Circular or AR = 1	0.4485	0.1726	-0.8970	3.7273
Elliptic AR = 2	0.4650	0.2645	-0.9301	16.8294
Elliptic AR = 3	0.4726	0.3293	-0.9451	39.8109

Table 4.5 Power law fit for $D = 2b$

nozzle	St vs Fr		St vs Re	
	exponent (m)	Intercept (K_1)	exponent (n)	Intercept (K_2)
Circular or AR = 1	0.4485	0.1726	-0.8970	3.7273
Elliptic AR = 2	0.4650	0.1826	-0.9301	4.4163
Elliptic AR = 3	0.4726	0.1845	-0.9451	4.6984
All AR	0.4694	0.1916	-0.9387	4.7748

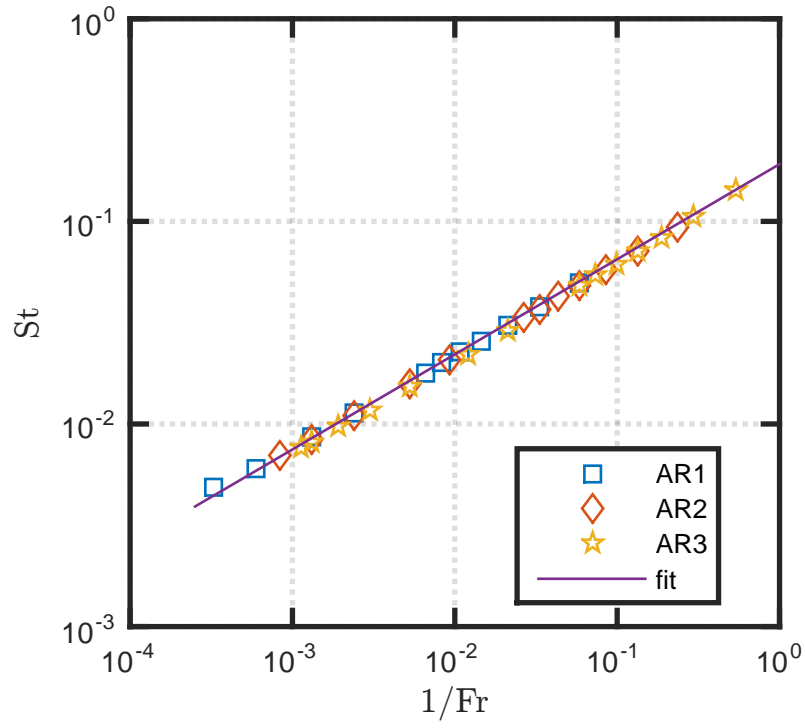


(a)

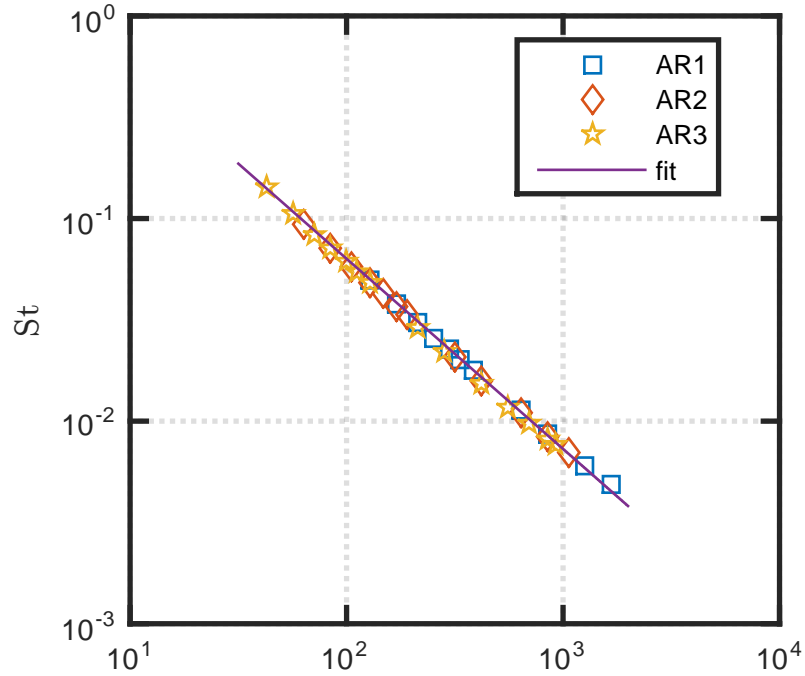


(b)

Fig. 4.11 (a) Strouhal number vs Froude number, (b) Strouhal number vs Reynolds number for natural oscillations in case of $AR = 1, 2, 3$ nozzles. The characteristic length D is $2a$.



(a)



(b)

Fig. 4.12 (a) Strouhal number vs Froude number, (b) Strouhal number vs Reynolds number with a common power law fit for natural oscillations in case of AR = 1, 2, 3 nozzles. The characteristic length D is $2b$.

Chapter 5

Forced Characteristics of Circular and Elliptic Diffusion Flame

In this chapter the results of the experiment performed to understand forced behavior of circular and elliptic diffusion flames are discussed. Chapter is concerned with discussing the dynamic behavior of different geometry flame (Circular and elliptic AR = 2,3) excited to different frequency and amplitude.

The experiments were performed with 99.5 % pure methane gas and the flames are sinusoidally excited by a speaker mounted at the bottom of the settling chamber, and their response is measured using a high speed camera via schlieren optical flow visualization technique. The camera settings used for this set of experiments are included in Table 5.1.

Table 5.1 Camera settings for acoustic excitation case

Frame rate	400 frames s^{-1}
Exposure time	1 μs
Resolution	384(w) x 720(h)
Field of view	44.64 D_{minor}
Image Type	8 bit monochrome
Image Scale	5.1867 pixel per mm
Video length	10148 frames
Post trigger	10148 frames
Auto exposure	Off

* D_{minor} is equal to the minor axis length for elliptical nozzles which in current study is same as 3 mm for all nozzles.

The flames are sinusoidally forced around their natural flickering frequency (F_n), near first super-harmonic ($2F_n$) and near the first subharmonic ($F_n/2$) in order to understand the change in the dynamic behavior of flames under acoustic excitation. In total three flames were

studied, one flame from each nozzle. Table 5.2 includes details about the flame parameters for all flames considered for forced response study.

Table 5.2 All flames used for acoustic excitation

Flame	Nozzle	Flow rate	Velocity	Re	Natural Frequency (F_n)
		SLPM	m/sec		Hz
1	Circular	0.7	1.6505	295.74	12.42
2	Elliptic AR = 2	0.8	0.9431	239	11.73
3	Elliptic AR = 3	0.9	0.7074	219.52	11.26

5.1 Forced response of circular nozzle flame

Methane reacting jet with circular nozzle (diameter = 3 mm) was forced sinusoidally with different amplitude and frequency in order to study its dynamic response to external excitations. When unforced the flame has a global mode at 12.42 Hz with weaker but similar peaks at harmonics. The presence of harmonics indicates that the natural global oscillations are not perfectly sinusoidal. The inner jet is forced at frequencies in the range [6.5 - 24.3 Hz]. The forcing amplitude¹ is varied until the flame liftoffs. The primary research question of this study is: how does the forced mode affect the natural mode? To answer that the study is divided mainly based on ratio of forcing frequency to natural frequency (F_f/F_n).

- Circular flame - 9 sets in F_f/F_n range 0.5 - 2 (60 experiments)
- Elliptic AR = 2 flame - 4 sets in F_f/F_n range 0.5 - 2 (25 experiments)
- Elliptic AR = 3 flame - 4 sets in F_f/F_n range 0.5 - 2 (25 experiments)

5.1.1 Forcing near the fundamental : F_n

Flame was forced at frequency = 11.8 Hz ($F_f/F_n = 0.95$) with amplitude range $0.025 \leq A \leq 0.125$ with an increment in amplitude of 25 mV. Figure 5.1 shows time series as well as power spectrum of intensity at all 5 amplitudes. For comparison flame without forcing case is also shown. When forced at low amplitude ($A = 0.025$ V) the flame responds at F_f as well as F_n , the power spectrum shows presence of both natural and forcing frequency although natural frequency is having more amplitude. Around these two frequencies there are multiple

¹Amplitude is in terms of the peak value of sine signal given to the speaker

peaks known as sidebands, which are generated by nonlinear interaction between the natural and forcing mode, as a result of this the beating phenomenon can also be seen in the time series signal for $A = 25$ mV (Fig. 5.1a).

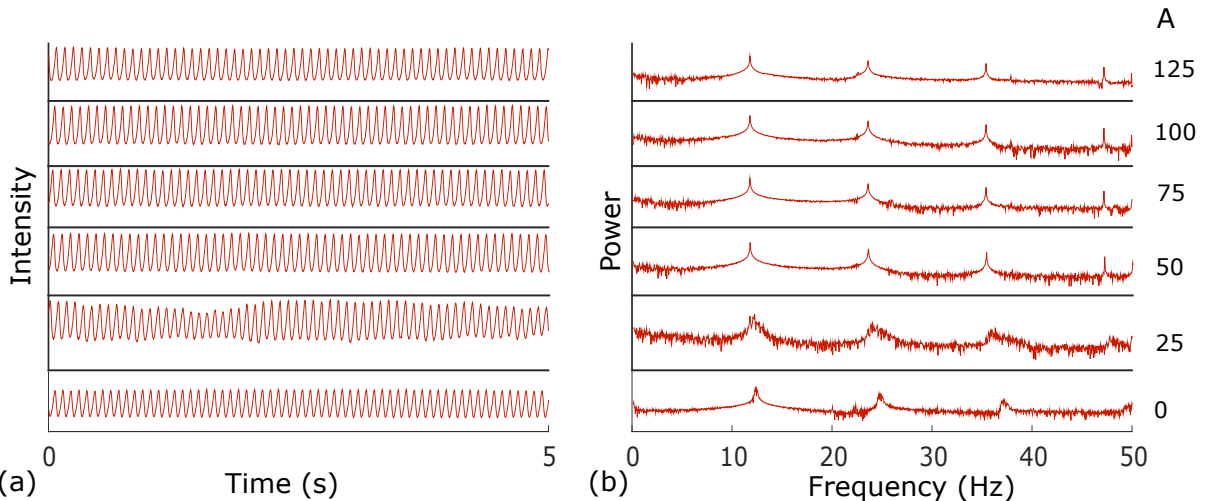


Fig. 5.1 (a) Time series (b) power spectrum of intensity for circular flame forced at $F_f = 11.8$ Hz, slightly below the natural frequency, $F_n = 12.42$ Hz: $F_f/F_n=0.95$. Data shown for five forcing amplitude ($0.025V \leq A \leq 0.125V$) and for the unforced case at $x/D = 10$ location. The amplitude shown is in mV.

As amplitude is increased from 25 mV to 50 mV, the power spectrum shows presence of only F_f and its super-harmonics ($2F_f, 3F_f, \dots$) with no signs of natural frequency in signal as can be seen in power spectrum in Fig. 5.1. As amplitude is increased beyond lock-in amplitude the power spectrum and time series of signal looks like unforced case with the only difference that the forcing frequency has replaced natural frequency.

Figure 5.2 shows phase space and return map reconstructed from time series data for $A = 0, 25, 50, 100$ mV. For unforced case the phase space shows a single closed curve pointing to presence of only one frequency (F_n) in system. At $A = 25$ mV the phase space shows a torus shape indicating presence of two frequencies in system, Poincaré map for this case shows a set of discrete points in 2D plane which actually indicates a mode locked (phase locked) state where the dynamics of the system recur after a time period decided by the combination of two rational frequencies. $A = 50$ mV shows a limit cycle in phase space and a single point in Poincaré map which confirms that the natural frequency has locked into forcing frequency and hence $A_{loc} = 50$ mV for this case. For amplitude higher than A_{loc} till $A = 125$ mV there is no change in the system dynamics and the flame stays locked in.

When forced at $F_f > F_n$ the similar features are observed. Figure 5.3 which is analogous to figure 5.1 shows time series and power spectrum for $F_f = 13.5$ Hz or $F_f/F_n = 1.0869$.

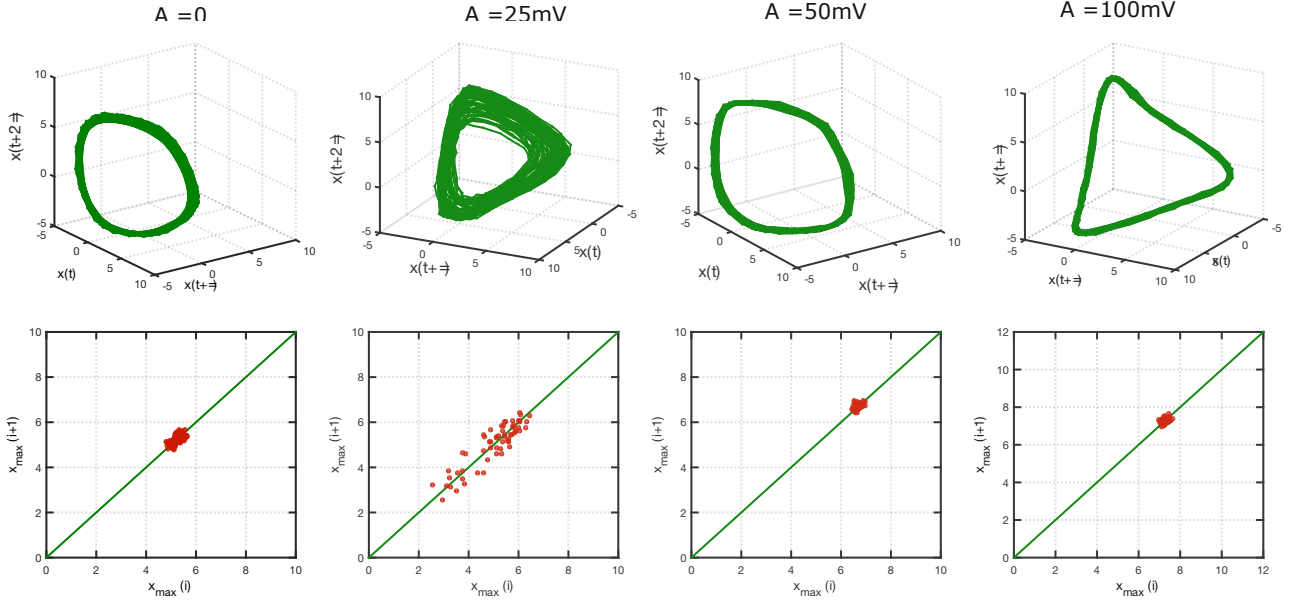


Fig. 5.2 (a) 3D phase portrait (b) Poincaré map for circular flame forced at $F_f = 11.8$ Hz, slightly below the natural frequency, $F_n = 12.42$ Hz: $F_f/F_n=0.95$. Data shown for three forcing amplitude in range $0.025 \leq A \leq 0.125$ and for the unforced case at $x/D = 10$ location. $A_{loc} = 50$ mV

A comparison of these two cases reveals both similarities and differences between forcing above and below the natural frequency.

Almost all the features seen for $F_f < F_n$ (figure 5.1) are seen for $F_f > F_n$ (figure 5.3) even the beating in the signal before lock-in and the mode locked state of dynamics are seen in non-linear time series analysis. As for differences the lock-in amplitude in case of $F_f > F_n$ is 75 mV which is higher compared to case when $F_f < F_n$. This follows the observations of Li (2012) where they observed that the amplitude for lock-in varies in proportion to $|F_f - F_n|$ on both side of $F_f/F_n = 1$.

5.1.2 Forcing near the first subharmonic : $F_n/2$

Figure 5.4 shows time series and power spectrum when excited at $0.10V \leq A \leq 0.450V$. For comparison signal and its FFT without forcing is also shown at bottom of fig. 5.4. When forced at $A = 100$ mV the flame responds to both forcing and natural frequency as expected, there is beating in signal as well as spectral peaks at $F_n - F_f = 5.92$ Hz and further interaction occur between natural frequency and beat frequency (5.92 Hz) which leads to a spectral band near F_n and its super-harmonics.

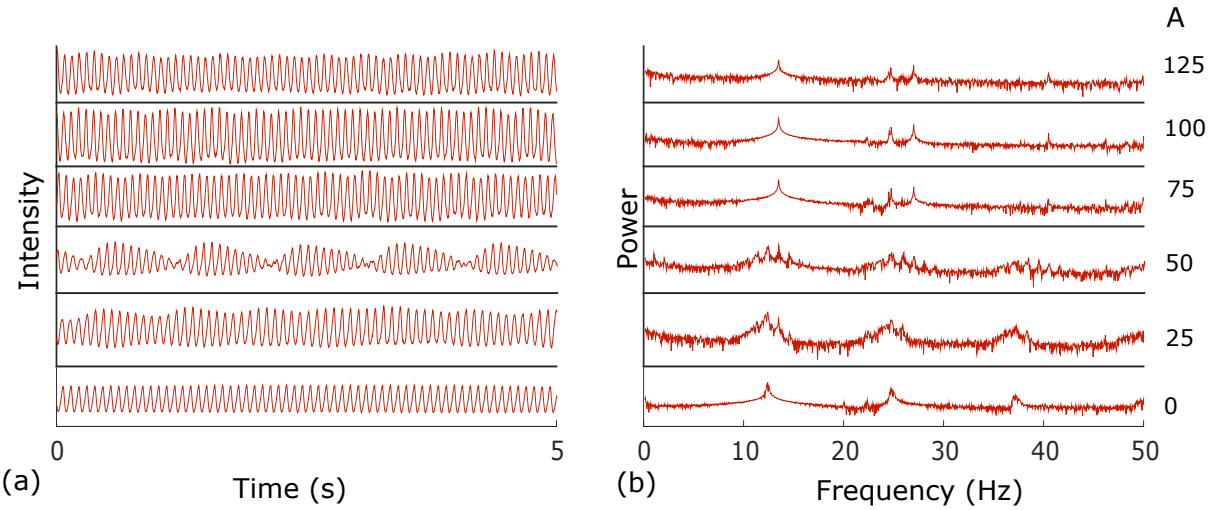


Fig. 5.3 (a) Time series (b) power spectrum of intensity for circular flame forced at $F_f = 13.5$ Hz, slightly above the natural frequency, $F_n = 12.42$ Hz: $F_f/F_n = 1.0869$. Data shown for five forcing amplitude ($0.025V \leq A \leq 0.125V$) and for the unforced case at $x/D = 10$ location. The amplitude shown is in mV.

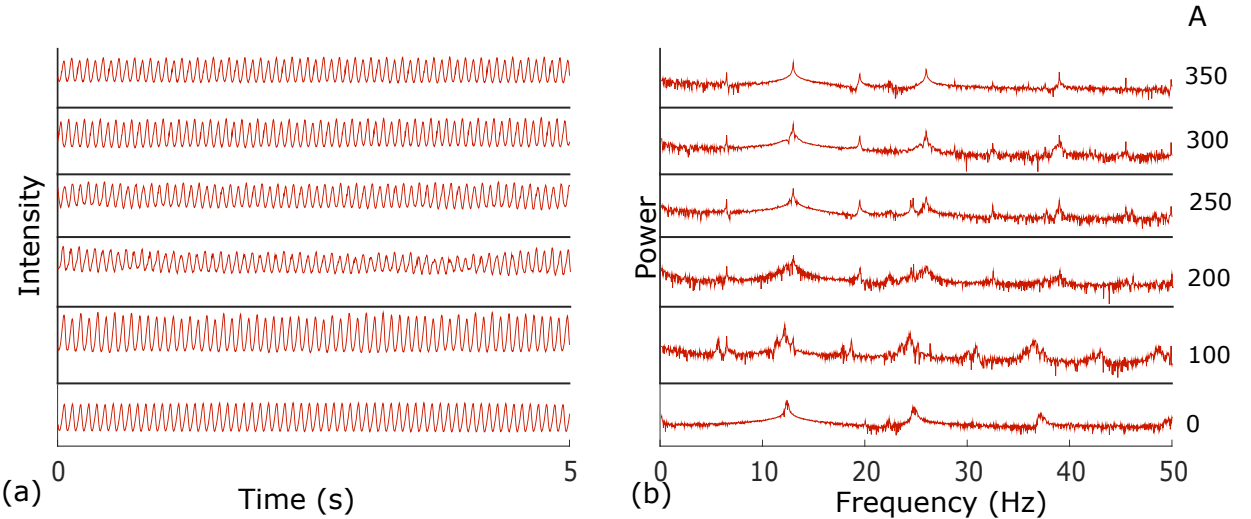


Fig. 5.4 (a) Time series (b) power spectrum of intensity for circular flame forced at $F_f = 6.5$ Hz, slightly above the first subharmonic of natural frequency, $F_n = 12.42$ Hz: $F_f/F_n = 0.523$. Data shown for five forcing amplitude ($0.10V \leq A \leq 0.45V$) and for the unforced case at $x/D = 10$ location. The amplitude shown is in mV. $A_{loc} = 300$ mV

From figure 5.5, looking at the phase space and Poincaré map at forcing amplitude = 100 mV we see that the system has gone in to mode locked from limit cycle at $A = 0$ V where the forcing and the natural mode competing for control of the oscillations. Further increasing

the amplitude ($A = 0.1 \text{ V} - 0.25 \text{ V}$) causes the phase portrait to break into two close curves which indicates a period doubling oscillations. From power spectrum it can be observed that the flame gets locked in with Frequency = 13 Hz rather than with 6.5 Hz even though the forcing frequency is 6.5 Hz. This phenomenon leads to highest power of $F = 13 \text{ Hz}$ in power spectrum and hence it acts as the dominant frequency which causes $F = 6.5$ (which is half of 13 Hz) to appear as a subharmonic of locked in frequency (13 Hz) and this leads to the system being in a period 2 oscillations state. At 300 mV amplitude Poincaré map (Fig. 5.5) shows two discrete points which indicates lock-in of natural mode with first super-harmonic of forcing frequency. It was observed by [Li \(2012\)](#) that further increasing the amplitude will again lead to period doubling oscillations but more experiments need to be done before concluding that in this case.

5.1.3 Forcing at $F_f/F_n = 0.8454$ or $F_f = 10.5 \text{ Hz}$

When the circular flame was forced at $F_f = 10.5 \text{ Hz}$ and at $0.10V \leq A \leq 0.70V$ the power spectrum shows non-linear interaction of natural and forcing frequency which causes the spectral peaks around fundamental as well as forcing frequency as can be seen in Fig. 5.6. A beat frequency at $|F_n - F_f|$ appears in power spectrum and the beating can be seen in corresponding time series signal. Figure 5.7 shows phase space and Poincaré map for five forcing amplitude and unforced case. When $0.10V \leq A \leq 0.30V$, the Poincaré map shows a circle which indicates quasi-periodic state of the system. As we further increase the amplitude the circle in Poincaré map breaks to a set of discrete points which occurs when the system is in phase locked state, so to summarize as we excite the flame at $F_f = 10.5 \text{ Hz}$ the system moves from limit cycle to phase locked through quasi periodic state for $0.10V \leq A \leq 0.70V$

If we take a closer look at the power spectrum at forcing amplitude $A = 300 \text{ mV}$ where the system starts developing from quasi-periodic to phase locked state, the two frequencies present in the system are 10.5 Hz and 12.58, meaning the natural frequency of the system has changed and it causes the ratio of two frequencies present to be rational which leads to a phase locked state while in quasi-periodic state the ratio of frequencies was an irrational number. So the reason for the state change of system from quasi-periodic to phase locked at higher amplitude is due to the evolution of natural frequency of the system to a new frequency where the ratio F_f/F_n becomes a rational number. Throughout the amplitude range shown the flame never gets locked into forcing frequency.

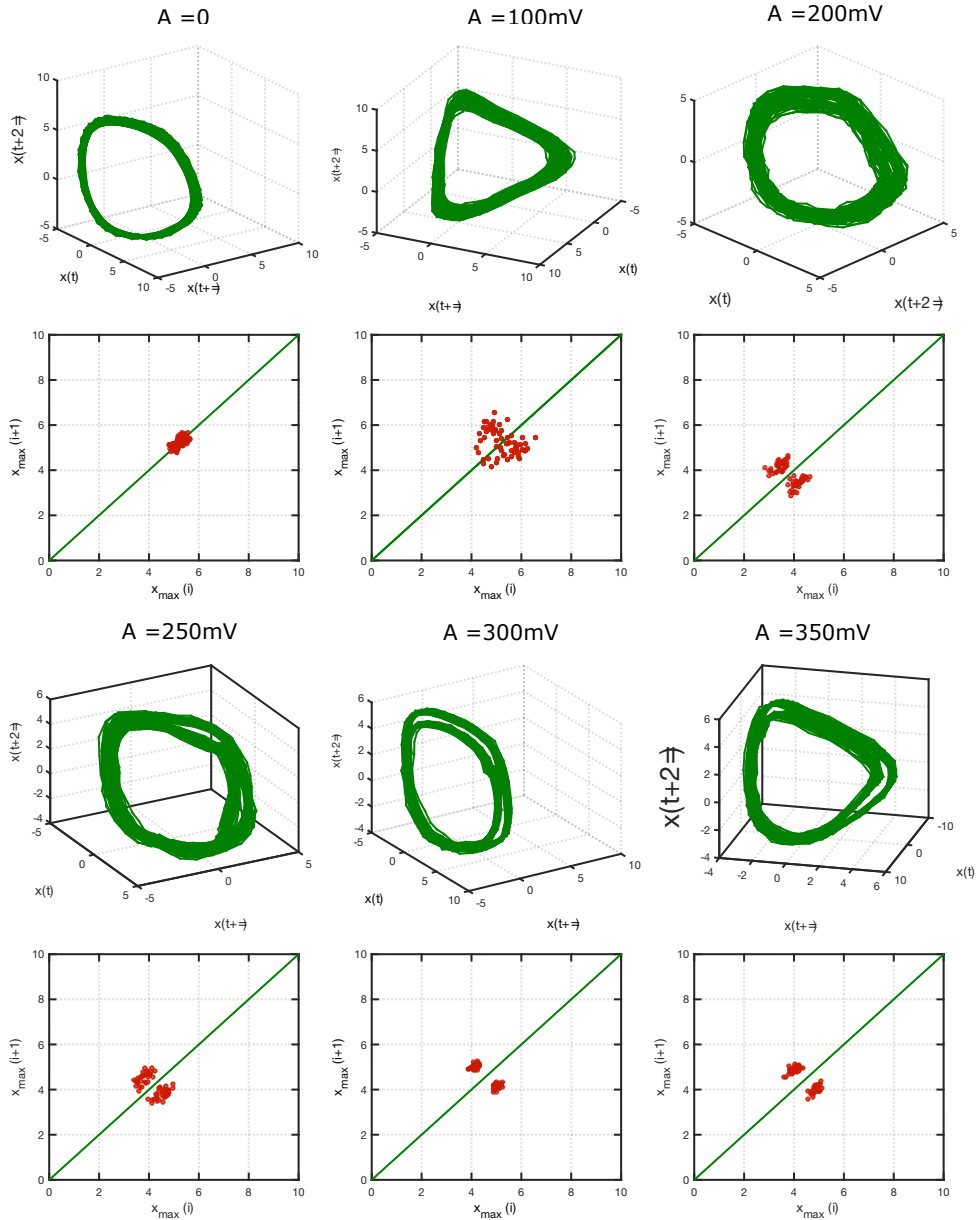


Fig. 5.5 (a) 3D phase portrait (b) Poincaré map for circular flame forced at $F_f = 6.5$ Hz, slightly above the first subharmonic of natural frequency, $F_n = 12.42$ Hz: $F_f/F_n=0.523$. Data shown for five forcing amplitude in range $0.1V \leq A \leq 0.35V$ and for the unforced case at $x/D = 10$ location. $A_{loc} = 300$ mV

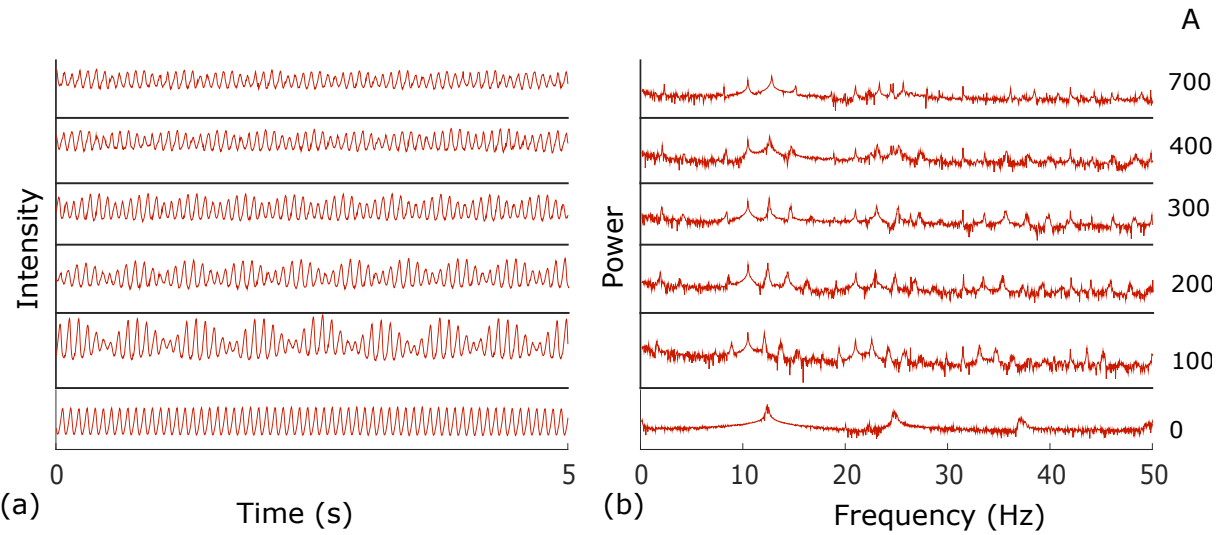


Fig. 5.6 (a) Time series (b) power spectrum of intensity for circular flame forced at $F_f = 10.5$ Hz; $F_f/F_n = 0.523$. Data shown for five forcing amplitude ($0.10V \leq A \leq 0.70V$) and for the unforced case at $x/D = 10$ location. The amplitude shown is in mV.

5.2 Forced response of elliptic nozzle flame

5.2.1 Forcing near the fundamental : F_n

When flame 2 (AR=2, Re = 239) was forced at $F_f = 12.6$ Hz, the response of flame was similar to the forcing response in case of flame 1 (circular nozzle). When unforced the flame shows global oscillations at 11.73 Hz. When forced at $A = 50$ mV the power spectrum in Fig. 5.8 shows the interaction between forcing and fundamental which leads to spectral peaks and beating in time series signal. Further increasing the amplitude causes the flame to get lock into forcing frequency at $A = 100$ mV and the power spectrum shows no sign of natural frequency. The flame stays locked in for anymore increment in amplitude till $A = 200$ mV.

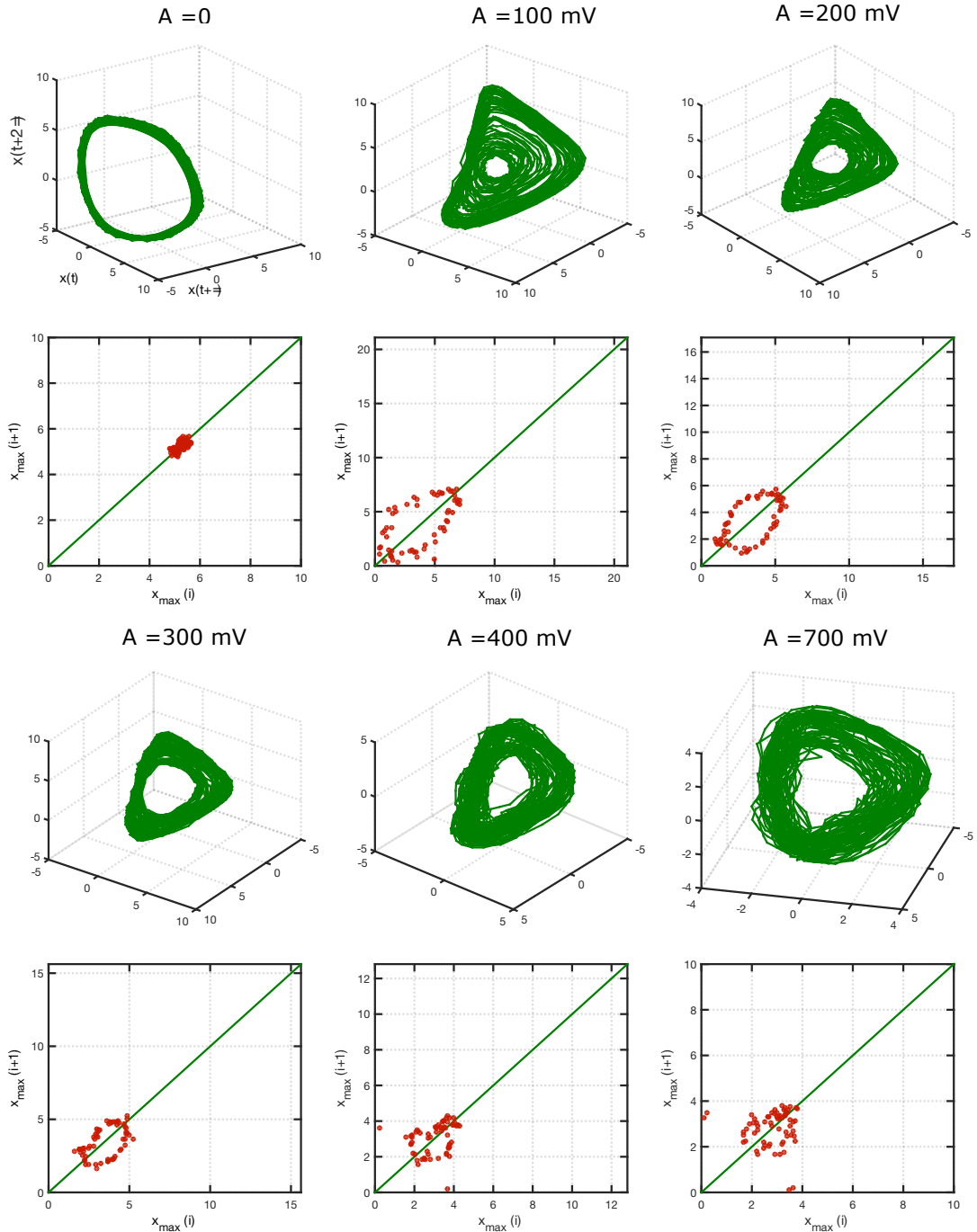


Fig. 5.7 (a) 3D phase portrait (b) Poincaré map for circular flame forced at $F_f = 10.5 \text{ Hz}$: $F_f/F_n = 0.8454$. Data shown for 5 forcing amplitude in range $0.1 \leq A \leq 0.7$ and for the unforced case at $x/D = 10$ location.

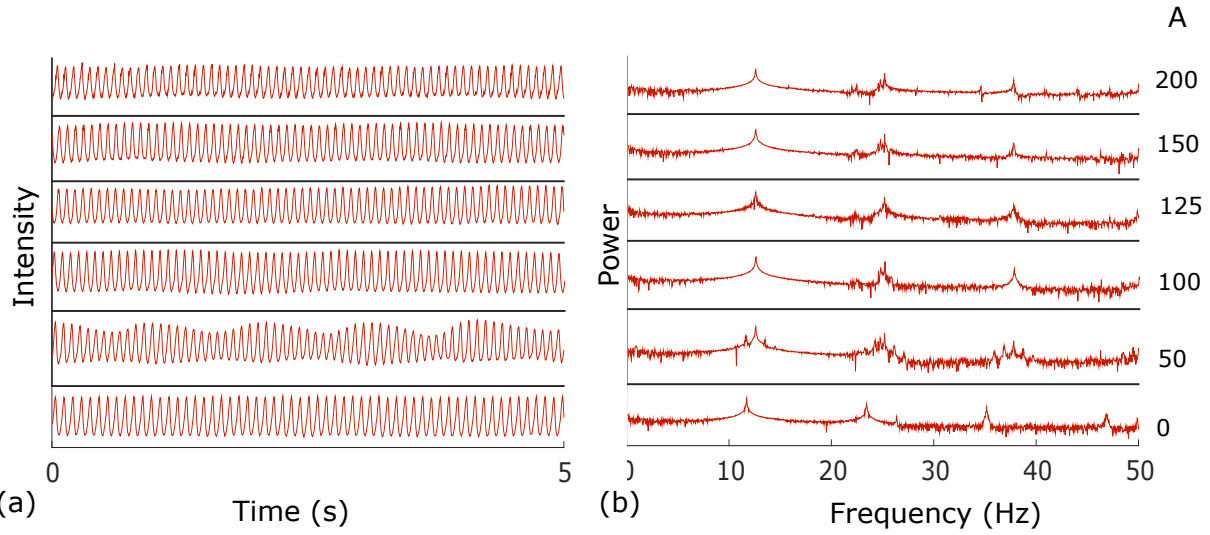


Fig. 5.8 (a) Time series (b) power spectrum of intensity for flame 2 (elliptic AR = 2 nozzle) when forced at $F_f = 12.6$ Hz: $F_f/F_n = 1.0742$. Data shown for five forcing amplitude ($0.05V \leq A \leq 0.20V$) and for the unforced case at $x/D = 10$ location. The amplitude shown is in mV. Lock-in occurs at $A_{loc} = 100$ mV

If we take a look at the non-linear time series analysis for this case, the topology of the system reveals that the system went from limit cycle at natural frequency to limit cycle at forced frequency through a phase locked state. Figure 5.9 shows phase space and Poincare map, at $A = 50$ mV the phase portrait shows toroidal structure and Poincare map shows set of discrete points which appears in case of phase locked state.

Similar response to forcing was observed when $F_f/F_n < 1$ for flame 2. Similarly for flame 3 (AR = 3 nozzle) the forcing response for $F_f/F_n < 1$ and $F_f/F_n > 1$ was similar to circular which is also similar to flame 2, with only difference in the lock-in amplitude. All these cases are not discussed here because they do not provide us any additional information about understanding of flame instability response to acoustic field.

5.2.2 Forcing near the first subharmonic : $F_n/2$

When unforced AR = 3 elliptic nozzle flame shows a global mode at $F_n = 11.26$ Hz. Forcing response of flame 3 near the first subharmonic of natural oscillation is shown in Fig. 5.10. When forced at amplitude in range $0.1V \leq A \leq 0.3V$ the interaction between natural and forcing leads to a beat frequency at $|F_n - F_f|$. Further interaction of this beat frequency with fundamental frequency and its super-harmonics causes the side band in power spectrum. At $A = 400$ mV the power spectrum is full of peaks because of another beat frequency caused by interaction of forcing and primary beat frequency ,i.e, $|F_f - (F_n - F_f)|$. Several combination

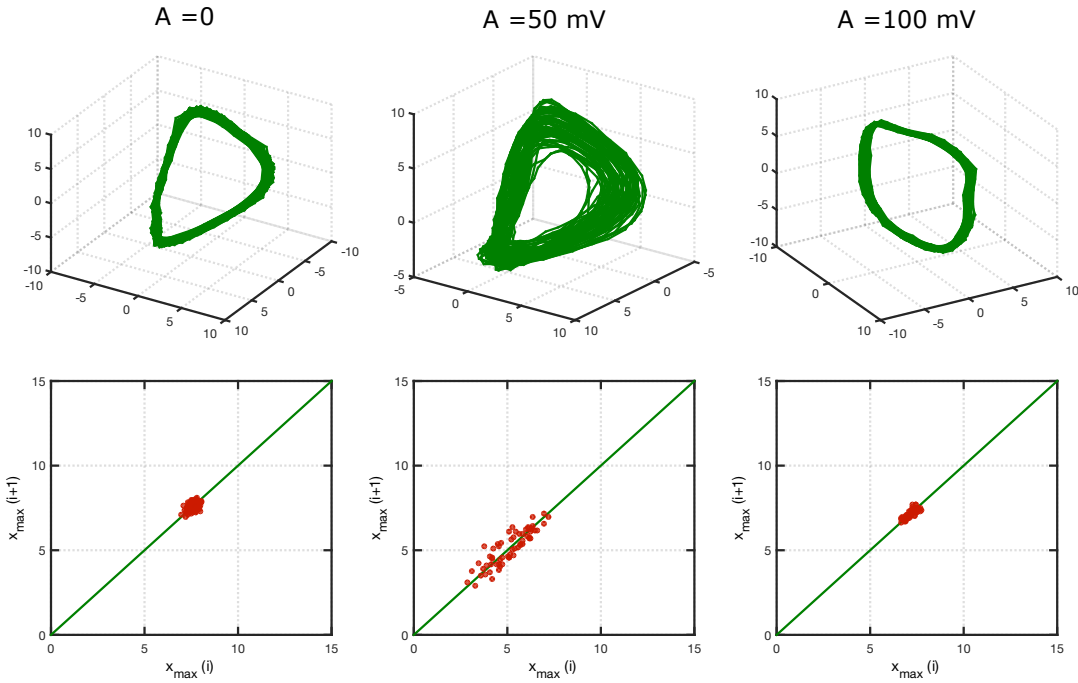


Fig. 5.9 (a) 3D phase portrait (b) Poincaré map for flame 2 ($AR = 2$, $Re = 239$) forced at $F_f = 12.6$ Hz: $F_f/F_n = 1.0742$. Data shown for lock-in, before lock-in amplitude and for the unforced case at $x/D = 10$ location.

of these primary and secondary beat frequency with natural and forcing frequency causes the train of spectral peaks and torus like structure develops in phase portrait. Poincaré map suggests system being in phase locked state. Further increasing the amplitude reduces the interaction between natural, forcing and beat frequencies and the spectral peak train starts to disappear as the forcing frequency takes over the flame dynamics and gets locked in at $A = 700$ mV. The surprising result is that in case of circular nozzle lock-in was achieved by a period doubling motion but here the forcing frequency and natural both are absent in spectrum. The first super-harmonic of forcing frequency is the dominant frequency and the system is in limit cycle state.

Similar results were observed for $AR = 2$ nozzle flame when forced near the first subharmonic of fundamental frequency, this dynamics differ from dynamics observed when circular flame was forced near subharmonic of its fundamental frequency. This can be interpreted in terms of stability of the system toward chaos. In physical system there exist a route to chaos through period doubling bifurcation, which was seen as a possibility in case of circular nozzle flames but in elliptical nozzle flames that bifurcation is not seen.

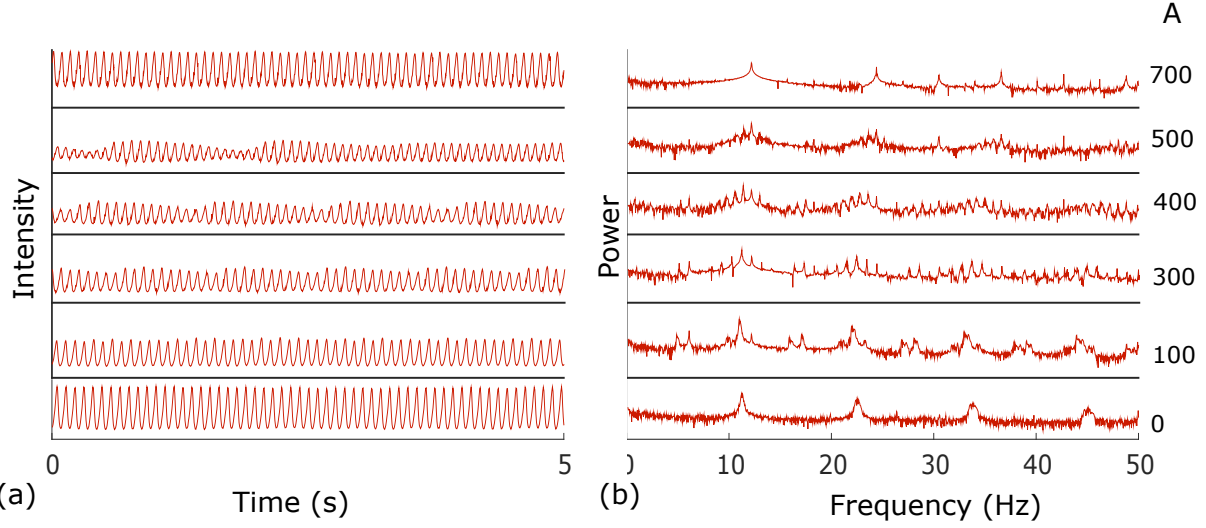


Fig. 5.10 (a) Time series (b) power spectrum of intensity for flame 3 (elliptic AR = 3 nozzle) when forced at $F_f = 6.1$ Hz: $F_f/F_n = 0.5417$. Data shown for five forcing amplitude ($0.1V \leq A \leq 0.7V$) and for the unforced case at $x/D = 10$ location. The amplitude shown is in mV. Lock in occurs at $A_{loc} = 700$ mV

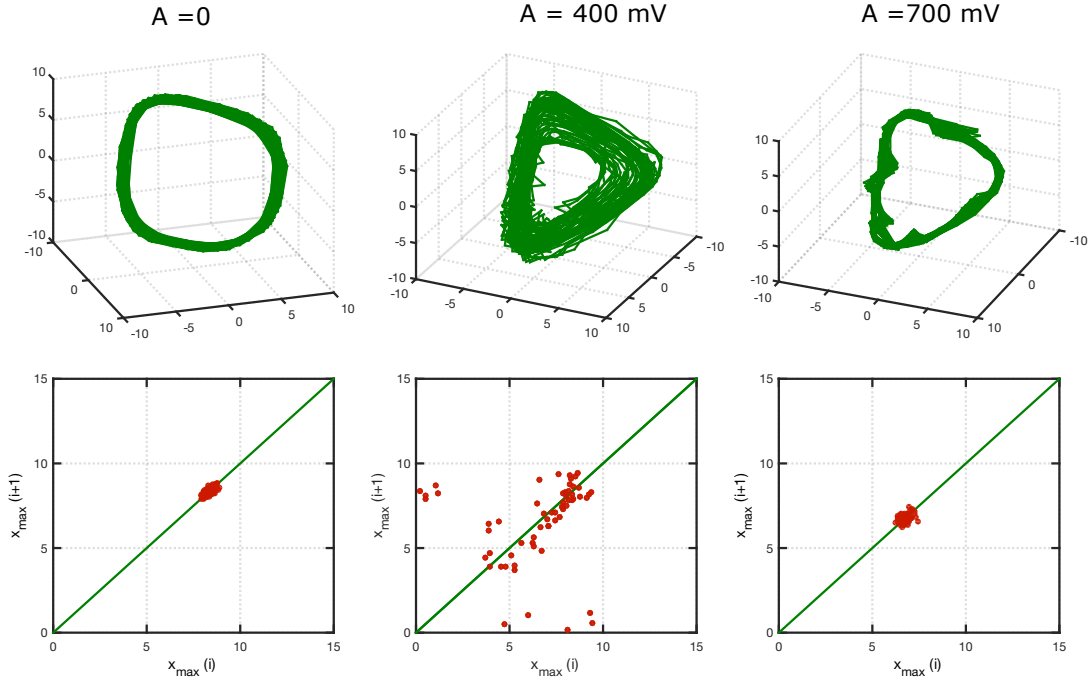


Fig. 5.11 (a) 3D phase portrait (b) Poincaré map for flame 3 (AR = 3, Re = 219.52) forced at $F_f = 6.1$ Hz: $F_f/F_n = 0.5417$. Data shown $A = 400, 700$ mV and for the unforced case at $x/D = 10$ location.

5.3 Results from DMD

DMD results for natural oscillation were discussed in section 4.4, same analysis can be done for any forcing case to see the spatial characteristics of forcing, natural oscillation modes and the modes which comes into dynamics due to their non-linear interactions like beat frequency. The results for one case will be discussed in this section but the same analysis can be applied to any forcing case if required.

DMD results shown below is for flame 1 ($AR = 1$, $Re = 295.74$) when forced at $F_f = 6.5$ Hz and $A = 100$ mV. FFT and non-linear time series analysis for this case is discussed in section 5.1.2. When unforced the flame shows an global mode at 12.42 Hz. A total of 1000 frames and the cross section shown in Fig. 4.7 were selected for DMD analysis. Figure 5.12 shows DMD spectrum and eigenvalues visualization in complex plane. Most of the modes lies on circle, since eigenvalue represent the temporal features of a mode, modes lying on unit circle has zero growth rate indicating suggests oscillations are saturated. The modes from DMD spectrum are selected to see their spatial features.

Figure 5.13 shows mean mode, mode corresponding to natural frequency and mode corresponding to forced frequency. Comparing the magnitude of mode 1 and mode 2 we can tell that the natural mode is dominant in downstream region while the forcing mode has a dominance in the center jet spatial location in terms of being active. Similarly phase plot tells us that all the modes are symmetric about Y axis and contribute to the symmetry in flame.

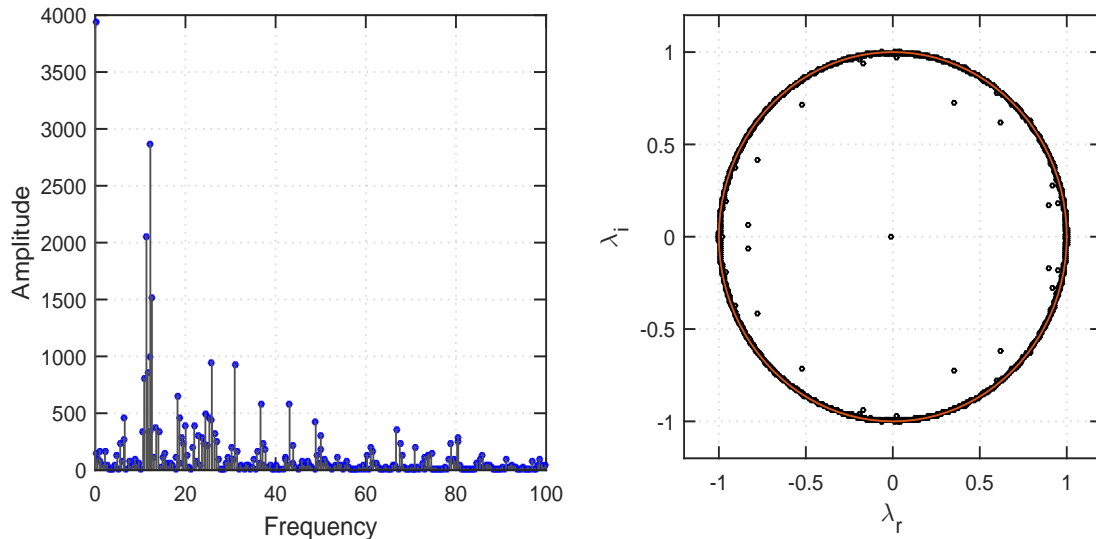


Fig. 5.12 (a) DMD spectrum, (b) eigenvalue visualization for flame 1 when forced at $F_f = 6.5$ Hz and $A = 100$ mV.

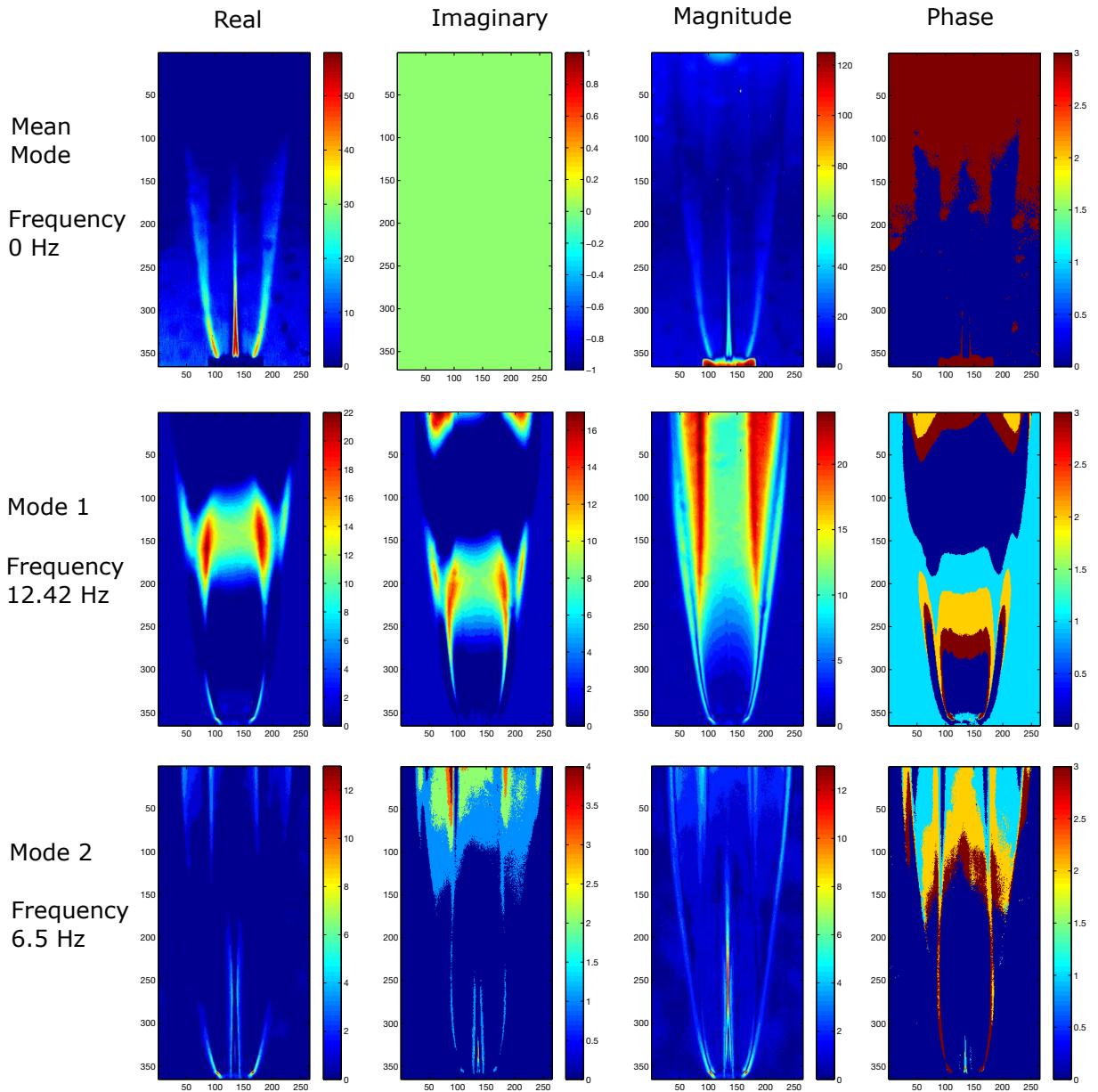


Fig. 5.13 Spatial characteristics of mean, natural and forcing modes for $AR=1$, $Re = 295.74$, major axis side case.

Chapter 6

Summary and Conclusion

This final chapter summarizes and concludes the results of this study and discusses about the research that can be continued in future.

6.1 Summary

The main objective of this study was to understand and compare behavior of elliptical diffusion flame to circular diffusion flame under natural as well as under acoustically forced conditions. A high speed schlieren flow visualization technique was used to capture the time resolved flame response. Time series data was generated from schlieren images for analysis which includes local decomposition techniques like FFT, Spectrogram. The modal data-based global decomposition technique - Dynamic Mode Decomposition was applied to time resolved frames to get more insight into the spatial characteristics of the different modes of flame flickering in natural as well as forced response cases. Non-linear time series analysis was used to understand the topology of the system during acoustic excitation and it helped in classify the type of interaction between forcing and natural frequency.

After a critical velocity of fuel at the nozzle exit, diffusion flames start to show buoyancy driven global oscillations. This study explored and compared the influence of velocity on frequency by changing the AR of nozzle. Three nozzles were considered for study with $AR = 1, 2, 3$ with same semi-minor axis length. It was found that the circular flames are the most dependent to change of fuel velocity whereas $AR = 3$ flame was least dependent. Another conclusion is that all the 3 nozzles have positive dependence of velocity, ie, on increasing the velocity the general trend showed increment in frequency except in few cases for $AR = 3$ where the frequency showed a drop. Dynamic mode decomposition was used to see the spatial characteristics of the modes corresponding to natural frequency and its super-harmonics.

In case of diffusion flames the correlation between Strouhal number and Froude number follows a power law fit. The exponent and the intercept of this fit were computed from experimental data for all three flames. When typical elliptic characteristic length ($D = 2\sqrt{ab}$) was used to compute the correlation, this scaling was not able to capture the behavior of different geometry nozzle flames under a single correlation but when it was taken as the minor axis of nozzle, the power law fit for all three flames collapses, strongly suggesting that the global instability which causes the flickering of diffusion flames depends only on the minimum distance between shear layers. Similar fit was also obtained for correlation between Strouhal number and Reynolds number. The buoyancy driven oscillation in diffusion flame starts to disappear because of turbulence as fuel flow rate was increased. It was observed and captured for all the three nozzles that just before disappearance of buoyancy driven oscillations the center jet of the flame shows meandering.

The main component of combustion process - a flame is capable to showing rich dynamics when forced acoustically. Experiments were carried out in order to understand how the flame dynamics changes when the flame is forced sinusoidally at the base of the settling chamber. The forcing response was captured for all three nozzle flames with excitation at different frequencies. For all 3 flames ($AR = 1, 2, 3$) when the flame was forced near the natural frequency of oscillations, the flame gets locked in to forcing frequency through a phase locked state. At low amplitude of forcing signal the dynamics showed competition between natural and forcing frequency for control of flame causing beating in time series signal and spectral peaks in power spectrum. Increasing the amplitude after a critical value caused the replacement of natural frequency with forcing frequency indicating lock in.

When circular flame was forced at $F_f/F_n = 0.8454$, Surprisingly the flame never gets locked in to the forcing frequency even till $A = 700$ mV which tells us that there is limit to deviation from $F_f/F_n = 1$ in which lock is possible. The interaction between natural and forcing showed that the system attained a quasi-periodic state at low amplitude, while at higher amplitude it changed to phase locked state. Reason for the transition was the shift of natural frequency. This aspect still needs further exploration.

When forced near the first subharmonic of natural frequency at high amplitude, the circular flame shows dominance of the first super-harmonic of forcing frequency which when looking at the topology of the system looked like a period doubling oscillations. More experiments need to be done to see if it further goes under period-doubling bifurcation route to chaos on increasing the amplitude. When all the 3 flames were excited near the first subharmonic of fundamental frequency, an important change in dynamics was observed between circular and elliptical nozzle flames. Circular flame showed a period-doubling route to lock in and possibility of period doubling bifurcation route to chaos while in case of

elliptic flame the system gets lock-in to the first super-harmonic of forcing frequency through a phase locked state.

6.2 Future Scope

This experimental study has answered few questions about natural and forced characteristic of circular and elliptic diffusion flames but it has raised few more question that needs to be explored in order to have a better understanding of acoustic interaction with natural instability in diffusion flame.

- More experiments needs to be carried out in order to get lock-in curve.
- How does the flames respond when the flame is excited at frequency much higher than the natural frequency? How does that response vary based on AR of nozzle?
- What happens if we excite the flame transversely instead of exciting it at the base.
- Are the results obtained in this experimental study also consistent with higher nozzles?

The same question can be asked in case of premixed flames. Finally a better understanding of what we observed from instability point of view in terms of control parameters and physical mechanisms.

References

- Baird, B. (2005), Effects of elliptical burner geometry on partially premixed gas jet flames in quiescent surroundings., Thesis.
- Balusamy, S., Li, L. K., Han, Z., Juniper, M. P. and Hochgreb, S. (2015), ‘Nonlinear dynamics of a self-excited thermoacoustic system subjected to acoustic forcing’, *Proceedings of the Combustion Institute* **35**(3), 3229–3236.
- Cao, L. (1997), ‘Practical method for determining the minimum embedding dimension of a scalar time series’, *Physica D: Nonlinear Phenomena* **110**(1-2), 43–50.
- Cetegen, B. and Dong, Y. (2000), ‘Experiments on the instability modes of buoyant diffusion flames and effects of ambient atmosphere on the instabilities’, *Experiments in Fluids* **28**(6), 546–558.
- Davidhazy, A. (2006), ‘Introduction to shadowgraph and schlieren imaging’.
- Gollahalli, S. R., Khanna, T. and Prabhu, N. (1992), ‘Diffusion Flames of Gas Jets Issued From Circular and Elliptic Nozzles’, *Combustion Science and Technology* **86**(1-6), 267–288.
- Golub, V. V. and Krivokoritov, M. S. (2015), ‘Dynamic response of jets and flame to an acoustic field’, *Journal of Physics: Conference Series* **653**(1), 012057.
- Hallberg, M. P. and Strykowski, P. J. (2008), ‘Open-loop control of fully nonlinear self-excited oscillations’, *Physics of Fluids* **20**(4), 041703.

- Hamins, A., Yang, J. C. and Kashiwagi, T. (1992), An experimental investigation of the pulsation frequency of flames, in ‘Symposium (International) on Combustion’, Vol. 24, Elsevier, pp. 1695–1702.
- Juniper, M. P., Li, L. K. and Nichols, J. W. (2009), ‘Forcing of self-excited round jet diffusion flames’, *Proceedings of the Combustion Institute* **32**(1), 1191–1198.
- Juniper, M. P. and Sujith, R. (2017), ‘Sensitivity and nonlinearity of thermoacoustic oscillations’, *Annual Review of Fluid Mechanics* (0).
- Kabiraj, L., Saurabh, A., Wahi, P. and Sujith, R. I. (2012), ‘Route to chaos for combustion instability in ducted laminar premixed flames’, *Chaos: An Interdisciplinary Journal of Nonlinear Science* **22**(2), 023129.
- Kabiraj, L. and Sujith, R. I. (2012), ‘Nonlinear self-excited thermoacoustic oscillations: intermittency and flame blowout’, *Journal of Fluid Mechanics* **713**, 376–397.
- Kantz, H. (1994), ‘A robust method to estimate the maximal lyapunov exponent of a time series’, *Physics letters A* **185**(1), 77–87.
- Krivokorytov, M. S., Golub, V. V. and Volodin, V. V. (2012), ‘The effect of acoustic oscillations on diffusion combustion of methane’, *Technical Physics Letters* **38**(5), 478–480.
- Li, L. (2012), Forcing of globally unstable jets and flames, PhD Thesis, University of Cambridge.
- Li, L. K. and Juniper, M. P. (2013), ‘Lock-in and quasiperiodicity in hydrodynamically self-excited flames: Experiments and modelling’, *Proceedings of the Combustion Institute* **34**(1), 947–954.
- Lin, Y.-T. and Chang, Y.-L. (1998), ‘Fundamental and subharmonic instability modes interaction in an acoustically controlled elliptic jet’, *Journal of the Chinese Institute of Engineers* **21**(1), 93–100.
- Mezić, I. (2013), ‘Analysis of Fluid Flows via Spectral Properties of the Koopman Operator’, *Annual Review of Fluid Mechanics* **45**(1), 357–378.

- Rowley, C. W., Mezić, I., Bagheri, S., Schlatter, P. and Henningson, D. S. (2009), ‘Spectral analysis of nonlinear flows’, *Journal of Fluid Mechanics* **641**, 115.
- Schmid, P. J. (2010), ‘Dynamic mode decomposition of numerical and experimental data’, *Journal of Fluid Mechanics* **656**, 5–28.
- Schmid, P. J., Li, L., Juniper, M. P. and Pust, O. (2010), ‘Applications of the dynamic mode decomposition’, *Theoretical and Computational Fluid Dynamics* **25**(1-4), 249–259.
- Settles, G. S. (2001), *Schlieren and shadowgraph techniques: visualizing phenomena in transparent media*, Experimental fluid mechanics, Springer, Berlin. OCLC: 248149245.
- Settles, G. S. and Hargather, M. J. (2017), ‘A review of recent developments in schlieren and shadowgraph techniques’, *Measurement Science and Technology* **28**(4), 042001.
- Strang, G. (2003), *Introduction to Linear Algebra*, Wellesley-Cambridge Press.
- Taira, K., Brunton, S. L., Dawson, S. T. M., Rowley, C. W., Colonius, T., McKeon, B. J., Schmidt, O. T., Gordeyev, S., Theofilis, V. and Ukeiley, L. S. (2017), ‘Modal Analysis of Fluid Flows: An Overview’, *arXiv:1702.01453 [physics]* .
- Takens, F. (1981), Detecting strange attractors in turbulence, in ‘Dynamical systems and turbulence, Warwick 1980’, Springer, pp. 366–381.
- Tropea, C., Yarin, A. L. and Foss, J. F. (2007), *Springer Handbook of Experimental Fluid Mechanics*, Springer Science & Business Media.
- Tu, J. H., Rowley, C. W., Kutz, J. N. and Shang, J. K. (2014), ‘Spectral analysis of fluid flows using sub-Nyquist-rate PIV data’, *Experiments in Fluids* **55**(9), 1805.
- Tu, J. H., Rowley, C. W., Luchtenburg, D. M., Brunton, S. L. and Kutz, J. N. (2014), ‘On Dynamic Mode Decomposition: Theory and Applications’, *Journal of Computational Dynamics* **1**(2), 391–421. arXiv: 1312.0041.
- Wang, Q., Zhang, Y., Tang, H. J. and Zhu, M. (2012), ‘Visualization of Diffusion Flame/Vortex Structure and Dynamics Under Acoustic Excitation’, *Combustion Science and Technology* **184**(10-11), 1445–1455.

- Wolf, A., Swift, J. B., Swinney, H. L. and Vastano, J. A. (1985), ‘Determining lyapunov exponents from a time series’, *Physica D: Nonlinear Phenomena* **16**(3), 285–317.
- Zhu, Y., Zhang, Y., Xiao, W., Hu, Y., Wang, D., Zhao, X. and Ye, X. (2016), ‘Reducing the radiation influence of self-luminous object on schlieren imaging via spatial filtering’, *Optik - International Journal for Light and Electron Optics* **127**(3), 1471–1473.

Appendix A

Additional non-linear time series analysis tools

A.0.1 Lyapunov Exponent

Lyapunov exponents determine the rate of divergence or convergence of initially nearby trajectories in phase space. In general, an m-dimensional system has m different Lyapunov exponents λ_i , where $i = 1, 2, \dots, m$. The most important of these is that the largest Lyapunov exponent λ_{max} , uniquely determines whether the system is chaotic or not. If $\lambda_{max} > 0$, two initially nearby trajectories of the attractor diverge exponentially fast as time progresses, constituting the extreme sensitivity to changes in initial conditions, which is the hallmark of chaos. Thus, for our purposes it suffices to constrain the analysis solely to the largest Lyapunov exponent.

Wolf's Method (1984)

¹

1. First step is to find the nearest neighbour to initial point and let the euclidean distance between them be L_0 .
2. Iterate both points forward for a fixed evolution time t_{evol} , which should be of the same order of magnitude as the embedding delay τ , and let the final distance between points be L_{evol} .
3. After each t_{evol} a replacement step is attempted in which we look for a new point in the embedding space whose distance to the evolved initial point is as small as possible,

¹Wolf et al. (1985)

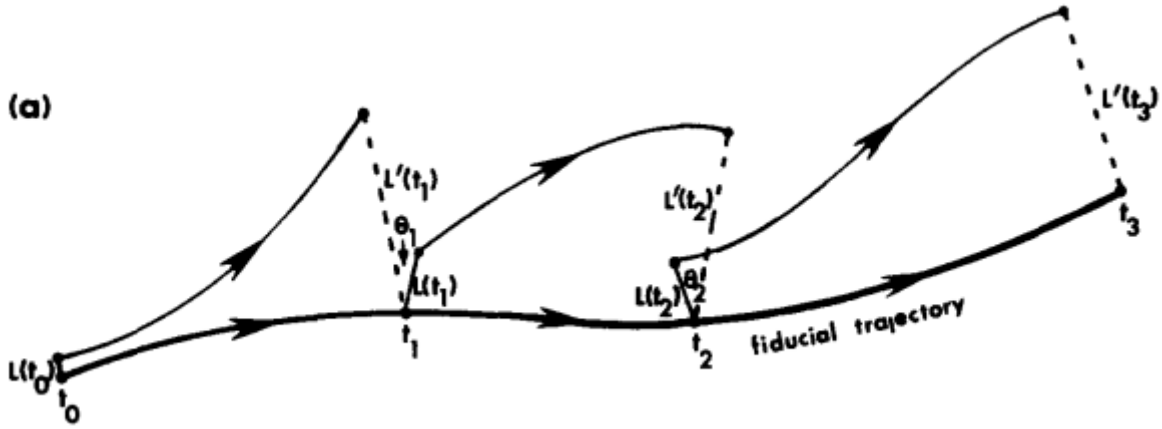


Fig. A.1 Illustration of procedure for calculating Lyapunov exponent. Taken from [Wolf et al. \(1985\)](#)

under the constraint that the angular separation between the evolved and replacement element is small. This procedure is repeated until the initial point reaches the end of the time series. Finally, λ_{max} is calculated according to the equation A.1

$$\lambda = \frac{1}{M * t_{evol}} \sum_{i=1}^{i=M} \ln \frac{L_{evol}^i}{L_0^i} \quad (\text{A.1})$$

Where M is the total number of replacement steps.

Algorithm by Rosenstein (1993) and Kantz (1994)

²

Choose a point S_j of the time series in embedding space and select all the neighbours with distance smaller than ε . Compute the average over the distances of all neighbours to the reference part of the trajectory as a function of relative time (Δn). The logarithm of the average distance at time Δn is effective expansion rate over the time span Δn . Repeating this for very many values of j , the fluctuation of the effective expansion rates will average out. Thus one has to compute:

$$S(\Delta n) = \frac{1}{N} \sum_{j=1}^{j=N} \ln \left(\frac{1}{|\cup(S_j)|} \sum_{S_n \in \cup(S_j)} |S_{j+\Delta n} - S_{n+\Delta n}| \right) \quad (\text{A.2})$$

Where,

- $\cup(S_j)$ is the neighbourhood of S_j with diameter ε .

²[Kantz \(1994\)](#)

- N is the number of data points
- Variables are Δn , embedding dimension (d) and ε
- The quantity $S(\Delta n)$ scales linearly with Δn with a slope corresponding to maximum lyapunov exponent.

Appendix B

Experimental parameters for natural oscillations case.

Table B.1 Experimental parameters with $D = 2\sqrt{ab}$ for natural oscillations. Bold indicated cases are the ones selected for acoustic excitation.

Flow rate (SLPM)	AR = 1 nozzle		AR = 2 nozzle		AR = 3 nozzle	
	Re	Fr	Re	Fr	Re	Fr
0.3	126.74	17.00	89.62	3.00	73.17	1.09
0.4	168.99	30.22	119.49	5.34	97.56	1.93
0.5	211.24	47.22	149.37	8.34	121.96	3.02
0.6	253.49	68.00	179.24	12.02	146.35	4.36
0.7	294.74	92.56	209.12	16.36	170.75	5.94
0.8	337.98	120.89	238.99	21.37	195.13	7.75
0.9	380.23	153.01	268.86	27.05	219.52	9.81
1.5	633.72	425.03	448.11	75.13	365.88	27.26
2.0	844.96	755.61	597.48	133.57	487.84	48.47
3.0	1267.5	1700.00	896.22	300.54	731.76	109.06
4.0	1689.9	3022.50	1195	534.30	975.68	193.89
5.0	-	-	1493.4	834.84	1219.6	302.95
6	-	-	-	-	1463.5	436.25
6.5	-	-	-	-	1585.5	511.99

All cases shown in table B.1 are done for both major and minor side schlieren visualization in case of elliptic nozzle.